Geophysical Journal International

Geophys. J. Int. (2022) **231,** 835–855
Advance Access publication 2022 June 16
GJI Geomagnetism, Rock Magnetism and Palaeomagnetism

https://doi.org/10.1093/gji/ggac224

An enigma in rock magnetism: can microstructures in magnetite cause a threefold increase in the efficiency of NRM acquisition in the Stardalur Basalts?

Suzanne A. McEnroe, Nathan Church, Karl Fabian, Marianne F. Stange and Antonius T. J. van Helvoort

*Norwegian University of Science and Technology, N-*7491 *Trondheim, Norway. E-mail: suzanne.mcenroe@ntnu.no*

Accepted 2022 June 14. Received 2022 June 2; in original form 2022 January 19

SUMMARY

Quaternary lavas of the Stardalur Caldera, 20 km northeast of Reykjavik, Iceland, create a 27 300 nT magnetic anomaly visible in both ground and aeromagnetic surveys. Here, we provide a comprehensive mineralogical and rock magnetic data set to analyse NRM intensities and Koenigsberger ratios of 57 drill-core samples from the critical zone (CZ) of the anomaly high at depths between 41 and 131 m. This extends previous studies and verifies that the anomaly is due to an unusually high intensity of remanent magnetization carried by magnetite. The NRM of the CZ samples was acquired during the Olduvai subchron in a field of at most today's strength. NRM intensities range from 20 to 128 A m^{-1} with a median of 55 A m^{-1}, and an average of 61 A m^{-1}, respectively, approximately 13–15 times higher than in typical Icelandic basalts (AIB) with an NRM intensity of 4 A m^{-1}. Our new data set shows that the magnetite concentration throughout the CZ basalts is at most twofold higher than in AIB lavas. New data on domain state and TRM efficiency prove that these properties account for an additional factor of at most 2.3. Because magnetite is the most abundant remanence carrier in rocks on Earth, and its remanence acquisition is considered to be extremely well understood, we assert that the remaining discrepancy is a critical enigma in rock magnetism. Results from scanning electron microscopy show that a significant fraction of all CZ magnetite particles have dendritic shapes with grain sizes <1 μm, indicating rapid crystallization. Most large magnetite grains are heavily subdivided by very fine oxidation-exsolution lamellae of ilmenite, and subordinate amount of exsolved spinel as needles, blebs and blades. These common microstructures found throughout the CZ subdivide the initially homogeneous mineral into separate cubicles, here denoted as *compartments*. The magnetite compartments then have sizes below 1 μm. Hysteresis data, Preisach maps and FORC data consistently confirm that the coercivity distribution is dominated by values above 10 mT, such that multidomain behaviour is of little relevance in the CZ. Between 5 and 20 per cent of the IRM is carried by coercivities above 100 mT, which for magnetite indicates unusually high anisotropy effects in the individual particles. Based on the quantitative analysis of all magnetic contributions to the NRM, we can demonstrate that the average efficiency of NRM acquisition in the CZ Stardalur basalts must be at least a factor 3 higher than in typical basalts. We speculate that this is related to the observed focused compartment size distribution <1 μm, and indicates thermochemical remanence acquisition below the Curie temperature of magnetite. Yet, a detailed physical mechanism for the extreme overefficiency of NRM acquisition remains enigmatic.

Key words: Magnetic properties; Microstructure; Magnetic anomalies: modelling and interpretation; Magnetic mineralogy and petrology; Rock and mineral magnetism; Stardalur Iceland;.

1 INTRODUCTION

1.1 The Stardalur anomaly

Aeromagnetic surveys in Iceland have revealed magnetic anomalies that are commonly aligned parallel, or subparallel, to active or extinct spreading zones. These anomalies are typically associated with volcanic centres and extend over 5–10 km (Kristjánsson & Jónsson 2017). The largest magnetic anomaly associated with a volcanic centre in Iceland is the Stardalur volcano, part of the Esja volcanic region in southwest Iceland. Understanding the mechanisms by which such large remanent magnetic anomalies are created is a key task in rock and mineral magnetism, and we here argue that fundamental concepts for such an understanding are still missing.

In a comprehensive review paper on the Stardalur anomaly, Kristjánsson (2013) reports the current state of data analysis. Magnetic susceptibilities at Stardalur have an average value of 0.067 SI, which corresponds well to data of Búason (1971) and is approximately 2.5 times higher than the average magnetic susceptibility of 0.025 SI of exposed Tertiary lavas in Iceland. Vahle *et al.* (2007) reported NRM intensities on 9 basalt samples from the CZ, with an average of 62 A m^{-1} consistent with the data of Kristjánsson (2013) and Búason (1971). Based on Kristjánsson and Búason data the average Koenigsberger ratio of basalts from the CZ is $Q = \mathrm{NRM}/(\chi\ H_L) = 27$, where $H_\mathrm{L} = 52\ \mu$T is the local geomagnetic field intensity. In comparison, for exposed relatively unaltered Icelandic Tertiary lavas, the arithmetic average NRM intensity is approximately $\mathrm{NRM_{AIB}} = 4$ A m^{-1} (Kristjansson 2002) yielding Q ratios of 3.9. The average NRM intensity of 61 A m^{-1} in Stardalur CZ basalts in relation to $\mathrm{NRM_{AIB}}$ is by a factor $\Phi = 61/4 \approx 15$ higher.

A database of Icelandic basalts complied by Tonti-Filippini & Brown (2019) provides abundant NRM data, however it contains a limited amount of magnetic susceptibility data. The main aim of this paper is to provide a comprehensive, and systematic evaluation of new and existing mineralogic data and rock magnetic parameters in the CZ, to ensure that all relevant processes are quantitatively studied in a statistically representative way. By that, we extend and support previous investigations, though also find that a large fraction of the unusual NRM at Stardalur still escapes our theoretical insight.

1.2 Geological background

Volcanic activity in Esja region occurred in just over one million years during the lower part of the Matuyama reverse polarity epoch, except for the two short normal polarity events N3 and N2 (Friðleifsson & Kristjánsson 1972; Kristjánsson *et al.* 1980) which are considered to represent the Olduvai and Gilsa events, respectively. The majority of the lavas composing the Esja peninsula, were erupted by the Kjalarnes, Hvalfjordur and Stardalur volcanic systems, active at 2.8, 2.0 and 1.7 Ma respectively. The Esja volcanic succession is approximately 2.4 km thick, and it is dominated by tholeiites, olivine tholeiites and minor basaltic andesites, icelandites and rhyolites. The Stardalur basalts erupted in subaerial and subglacial conditions with at least three glaciations occurring during the life of the Stardalur Complex. The stratigraphic section is characterized by sequences of lava flows intercalated, with thick subglacial hyaloclastite units (Geirsdóttir *et al.* 2007). Stratigraphic correlations indicate that Esja unit 18 forms the base of the Stardalur volcano, unit 23 was emplaced after the collapse of the central Stardalur volcano, and units 25–26 correlate with the Stardalur rhyolites (Kristjánsson *et al.* 1980).

Geological mapping of the eroded Stardalur complex shows a 6.5-km-wide caldera with sheets, rhyolite and dolerite intrusions, and small plugs surrounding the caldera rim (Friðleifsson & Kristjánsson 1972; Friðleifsson & Tómasson 1972; Friðleifsson 1973). Pasquarè & Tibaldi (2007) provide detailed structural data on the faults and intrusions within the eroded Stardalur volcano. In the western section of the caldera there is a fault where hydrothermal fluids were pervasive, and the rocks are heavily altered. The southern half of the rim is covered by 'Reykjavik grey basalts', a lava sequence of Late Quaternary interglacial age which is widespread in this region.

The large positive magnetic anomaly at Stardalur is surrounded by reversely polarized rocks which create magnetic lineations of 20 km wide and –1.5 μT amplitude below background (Sigurgeirsson 1970–1985). A ground magnetic survey showed a peak intensity of 79 000 nT in the caldera which is 27 300 nT above the local IGRF field intensity of 51 700 nT in 1968 (Kristjánsson 1970). An aeromagnetic survey flown in 1970 measured a large magnetic anomaly in the vicinity of the caldera, though the exact shape and size of the Stardalur anomaly was not accurately determined due to the wide 4 km spacing of the flight lines. Later, in 2011 Kristjánsson carried out a ground-magnetic survey with a probe height of 2 m above ground to delineate better the shape of the main peak of the anomaly, and to improve estimates of the anomaly amplitude. A maximum peak value of 81 400 nT was determined in a background field of 51 750 nT (Kristjánsson & Jónsson 2017). Based on the average magnetic susceptibility of the Stardalur samples we estimate the contribution from induced magnetization to the anomaly is approximately 3600 nT. Kristjánsson (1970) estimated that the peak magnetic anomaly could be generated by a single body of 200×600 m size striking NE, with an upper surface at a depth of 50–70 m, and a total magnetization intensity of 50–60 A m^{-1} similar to the analysis of ground-survey data by Búason (1971) that yielded a magnetization estimate of 80 A m^{-1} and slightly different dimensions.

1.3 Magnetic susceptibility and NRM in relation to Icelandic basalts

Fig. 1(a) plots Kernel density distributions of Icelandic basalt NRM data. The black line represents NRM values from the Icelandic database. The red line displays the NRM distribution from the Stardalur drill core which occupies a distinct and isolated area due to the very high NRM intensities. In early Icelandic studies it was common practice to demagnetize samples to 10 mT prior to measuring the NRM to remove any viscous magnetization. The grey line in Fig. 1(a) represents a large number of NRM values after 10 mT blank demagnetization. This demagnetization places some limits on the comparison to the Stardalur NRMs, however we consider the grey data in Fig. 1(a) to provide reasonable background data. Twenty-four Stardalur samples previously AF demagnetized showed only a few percent of the NRM were removed by 10 mT AF step (see Vahle *et al.* 2007; Kristjánsson 2013, Fig. 6a). Because the shift between the black and the red distributions in Fig. 1(a) corresponds approximately to a factor $\Phi = 13$, we consider this the most realistic estimate for Φ.

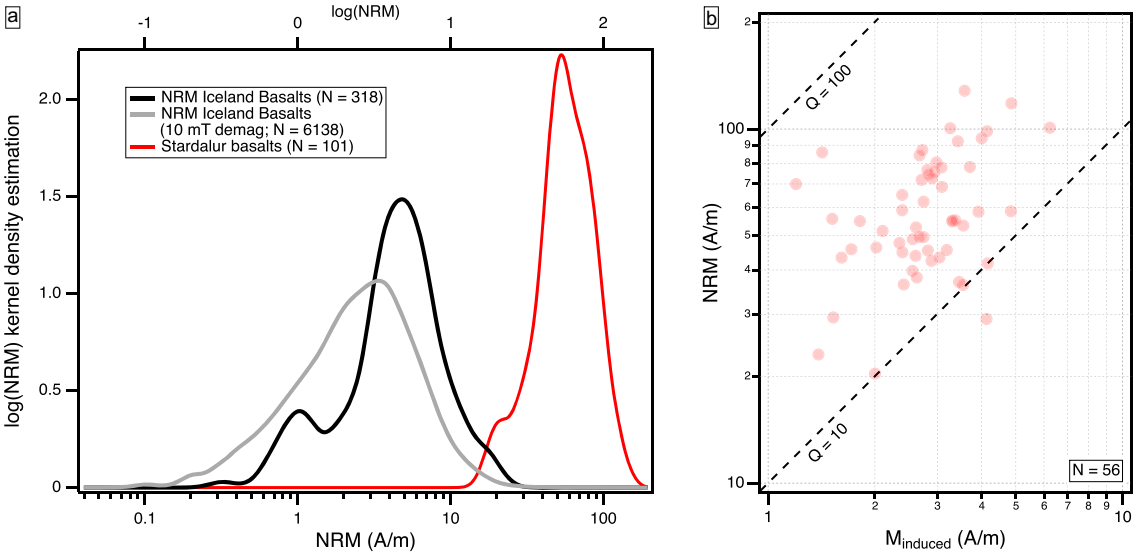

Figure 1. Left-hand panel (a) Kernel density distributions of Icelandic basalt NRM data from (http://www.icepmag.org) and the Stardalur data. Right-hand panel (b) Bilogarithmic plot of NRM (A m^{-1}) versus induced magnetization (A m^{-1}) for the Stardalur basalt samples from the CZ.

Fig. 1(b) is a bilogarithmic plot of NRM (A m^{-1}) versus induced magnetization (A m^{-1}) based on measured magnetic susceptibility and assumed external field $H_0 = 50\ \mu$T. Dashed lines correspond to Koenigsberger Q ratios of $Q = 10$ and $Q = 100$. The line for $Q = 1$ would be parallel and start in the lower right corner of this plot, emphasizing that the samples carry a unusually high NRM for magnetite-bearing rocks, especially those that contain multidomain magnetite, which typically have $Q < 1$. Fine-grained basalts will have higher Q ratios, however, these are commonly below $Q = 10$. The Stardular samples have very high Q ratios for magnetite bearing rocks. In more oxidized rocks high Q ratios >10 are typically due to a combination of a high NRM coupled with very low magnetic susceptibility (Clark 1997; McEnroe & Brown 2000). In contrast, the Stardalur basalts have higher than normal magnetic susceptibilities for basalts, and therefore require significantly higher NRMs to produce the same Q ratios found in more oxidized rocks.

Vahle *et al.* (2007) provided magnetic properties of eleven Stardalur samples, of which nine derive from the CZ, reported mineral observations on six CZ samples, and additional details on four samples using the SEM. Here, we extend this, and other previous studies by adding rock and mineral magnetic properties of 59 CZ Stardalur samples, TRM efficiency data on 10 CZ samples, and detailed microscopy on 20 CZ samples from the 138 m vertical drill core located at the centre of the anomaly. Our aim is to quantitatively test the conclusion of Kristjánsson (2013) that the Stardalur anomaly is the coincidental result of several independent factors that all enhance the NRM of the remanence carriers. Based on our new comprehensive data set we find that this earlier conclusion accounts only for a fraction of the observed NRM, and that there remains a missing factor of approximately three which cannot be explained by any of the previously discussed mechanisms. We provide evidence that this factor is due to an unusual efficiency of NRM acquisition in the Stardalur magnetite. Because magnetite is the best studied magnetic mineral, this is a true enigma in rock magnetism, and its explanation may require a substantial extension and revision of the current concepts of NRM acquisition in magnetite dominated igneous rocks.

2 METHODS AND MATERIALS

2.1 Sample material

The sample material for this study was kindly provided by Leo Kristjánsson. It consists of 59 evenly distributed CZ subsamples from the original collection of the Stardalur drill core. A table of Kristjánsson's earlier NRM and magnetic susceptibility data for the Stardalur collection is compiled in Table S1.

2.2 Rock magnetic measurements

The densities of 57 samples were measured using a Mettler Toledo ML104 scale with density attachment. Samples were soaked in water for a minimum of 24 hr, and then weighed in air followed by weighing in water. Densities were calculated using the principle of Archimedes. Sample volumes are also determined during this procedure. Room-temperature magnetic susceptibility was measured on 56 samples in an alternating field of amplitude 80 A m^{-1} using a Sapphire Instrument susceptibility bridge. Background magnetic susceptibility was measured before and after each sample measurement. After the background correction, the volume magnetic susceptibilities were normalized by calibration to a specimen with known susceptibility and reference volume of $V_0 = 8$ cm^3 by multiplication with V_0/V_s, where V_s is the individual sample volume. This provides the true volume magnetic susceptibilities (SI). Six samples were demagnetized using an AGICO LDA5 AF demagnetizer. Isothermal magnetic data, hysteresis properties, FORC distributions, Preisach maps were measured using a Princeton Measurement Corp. MicroMag 2800 Vibrating Sample Magnetometer (VSM) at NTNU. Specimen chips were weighed prior to the measurement. This enables to transform the measured magnetic moments (Am^2) to weight specific magnetizations σ (Am^2 kg^{-1}) and after multiplication by sample density ρ to obtain volume normalized magnetizations M (A m^{-1}). Hysteresis loops and backfield curves were measured for 59 samples. The maximum field was set to 1 T, with field increments of 3 mT. These measurements after weight normalization provide the hysteresis parameters σ_s, σ_{rs}

($Am^2\,kg^{-1}$), H_c and H_{cr}. Measurements were corrected for diamagnetic and paramagnetic susceptibility by linearly fitting the upper hysteresis branch above 0.7 T. FORC distributions (Pike *et al.* 1999; Roberts *et al.* 2000) were measured on 22 samples representing the complete range of NRM values. The FORC measurement saturation field was set to +600 mT. The horizontal limit of the diagram was typically set to 300 mT. The field increment was set to 2.5–3 mT, with the exception of one, which had a field increment of 5 mT. Data were processed using FORCinel (Harrison & Feinberg 2008) and VARIFORC 'non-square' smoothing (Egli 2013). Remanent Preisach maps were obtained for eight samples at 25 °C following the method of Church *et al.* (2016). The magnetizations were acquired by applying and removing a maximal positive field, followed by applying and removing negative conditioning fields $H_a = -H_i$, for values 1 and up to a chosen parameter. We based the parameters set for these measurements on the shape of the remanence curves. The initial field was set to 0 T, and the final field between 500 and 850 mT. The averaging time was set to 2 s, and field increment was 0.5 mT. For 10 sample chips (average mass 36 mg), a TRM was imparted in the VSM by cooling the samples from 630 °C to room temperature at a rate of ≈40 °C min^{-1} in a $H_0 = 50\ \mu T$ applied field. The heating and cooling steps were conducted in a flowing helium atmosphere. Calculated TRM efficiencies TRM/M_s and TRM/M_{rs} are based on room-temperature TRM values and M_s and M_{rs} obtained from hysteresis loops of the same chip.

Temperature dependent magnetic susceptibility was determined using an AGICO MFK1–FA Kappabridge equipped with CS-4 furnace and CS-L cryostat using an AF-field amplitude of 200 A m^{-1} (0.25 mT). Typically 0.3–0.5 g of specimen powder was weighed into a test tube together with a thermometer. Measurements were performed in three steps: a low-temperature (LT) heating curve, a high-temperature (HT) heating and cooling curve, typically followed by a second LT heating curve. For LT runs, specimens were inserted into the cryostat, and cooled by liquid nitrogen. When the temperature of the sample reached –195 °C or 78 K, the liquid nitrogen was removed from the cryostat by argon gas. Magnetic susceptibility was then measured in incremental steps as it gradually heated up to room temperature (RT). For HT runs, magnetic susceptibility was measured incrementally as the sample was heated from RT up to 700 °C, and while it cooled down to RT again. The typical set up was a heating rate of 13.3 °C min^{-1} and 281 measurement steps. To prevent oxidation, high-temperature measurements were acquired in an argon gas atmosphere with a flow rate of 6–8 l hr^{-1}. Low-temperature MPMS measurements were made at the Institute for Rock Magnetism, Department of Earth and Environmental Sciences, Minneapolis, USA.

2.3 Microscopic methods

To characterize the mineralogy and microstructures throughout the CZ, a representative collection of twenty thin sections was selected that covers the complete depth range and all types of magnetic properties. Thin sections were examined by transmission and reflected light microscopy. Fourteen thin sections were further studied by SEM, and 6 were selected for electron microprobe (EMP) analyses, and one sample for a TEM study on magnetite–ilmenite microstructures. Electron Microprobe (EMP) and Scanning Electron Microscope (SEM) Analyses of plagioclase, pyroxene, ilmenite and magnetite phenocrysts were acquired on either a JOEL and CAMECA electron microprobe. The EMP beam has a minimum resolution of a 1 μm and an activation area of 3 μm. Backscattered electron imaging of thin sections was performed using a Hitachi SU-6600 field-emission source SEM at 20 kV accelerating voltage, and a Phenom CeB_6 desktop SEM at 10 kV. The TEM sample was prepared by focus ion beam liftout (30 kV Ga-FIB, FEI Helios) and studied in a Jeol 2100F transmission electron microscope (TEM). Imaging used a Gatan 2k Ultrascan CCD, and in scanning-TEM mode a 1 nm probe and an annular detector with inner angle of 50 mrad. Energy dispersive X-ray spectroscopy was performed by on 80 mm^2 silicon drift detector (SDD, Oxford Instruments) and the Oxford instruments Aztec package was used for data collection and processing. Scanning precession electron diffraction was collected with a nominal probe size of 1 nm and a precession angle of 0.7° and the pattern on the fluorescence screen recorded with a StingRay camera. Template matching was done in Nanomegas Index software.

3 RESULTS

3.1 Microscopy

The thin sections examined from the CZ contain plagioclase and clinopyroxene phenocrysts typically in abundances of 1–5 per cent. Plagioclase laths were up to 300 μm in length, and clinopyroxene grains were up to a few 100s of microns in size (Fig. 2a). In some thin sections the plagioclase phenocrysts have a skeletal morphology, and small glomerocrysts of plagioclase and clinopyroxene were observed. Large discrete magnetite grains ($\gg$50 μm) compose less than 0.05 per cent of the thin section(Figs 2a and b). Magnetite grains commonly contain abundant very fine trellis (111) oxidation exsolution lamellae of ilmenite, which result in subdivided areas of magnetite that typically are $<$1 μm in width. Magnetite grains with large sandwich laths of ilmenite (Figs 2g and h) were subordinate to magnetite grains with abundant trellis lamellae of ilmenite. Most magnetite grains also contained pleonaste ($MgAl_2O_4$-$FeAl_2O_4$) where the plane of exsolution is along the (100) spinel planes. Hercynite ($FeAl_2O_4$) blebs likely nucleated on the edges of ilmenite lamellae. Some discrete large magnetite grains had clear indications of very rapid growth as evidenced by the hopper structure (Figs 2e, f and i), a shape created when the crystal grows faster at the edges of each face than at the centre. In these thin sections both plagioclase and clinopyroxene phenocrysts contained inclusions of trapped liquid, now crystallized to glass (Fig. 2a) or a mixture of very fine-grained crystals and oxides. Some plagioclase grains have a skeletal structure and frequently the edges were ragged, and appeared out of equilibrium. Discrete large ilmenite grains are ubiquitous in many samples, usually with a morphology of blades, some $\gg$50 μm in length. We did not observe ilmenohematite in any thin section, which was previously reported by Vahle *et al.* (2007).

All samples have a very fine-grained matrix usually with some devitrified glass, and up to 10 per cent amygdules (filled vesicles), commonly $>$1 mm in diameter. Amygdules were commonly filled with chlorite, calcite and sulfides. Small hematite grains rimmed some amygdules (Fig. 2c). Matrix grains of plagioclase and clinopyroxene with an intergranular texture are common, as were magnetite and ilmenite. Dendritic magnetite grains can contain oxidation-exsolution lamellae of ilmenite, spinel (pleonaste) exsolution blebs, or needles(Figs 2d and j). The plane of exsolution is along the {100} spinel plane. Dendritic magnetite grains ranged from $<$1 to 10s μm in size, though the individual magnetite compartments which make up the dendritic pattern are of submicron size (Figs 2d and j). Magnetite in a skeletal herring-bone morphology was common in the

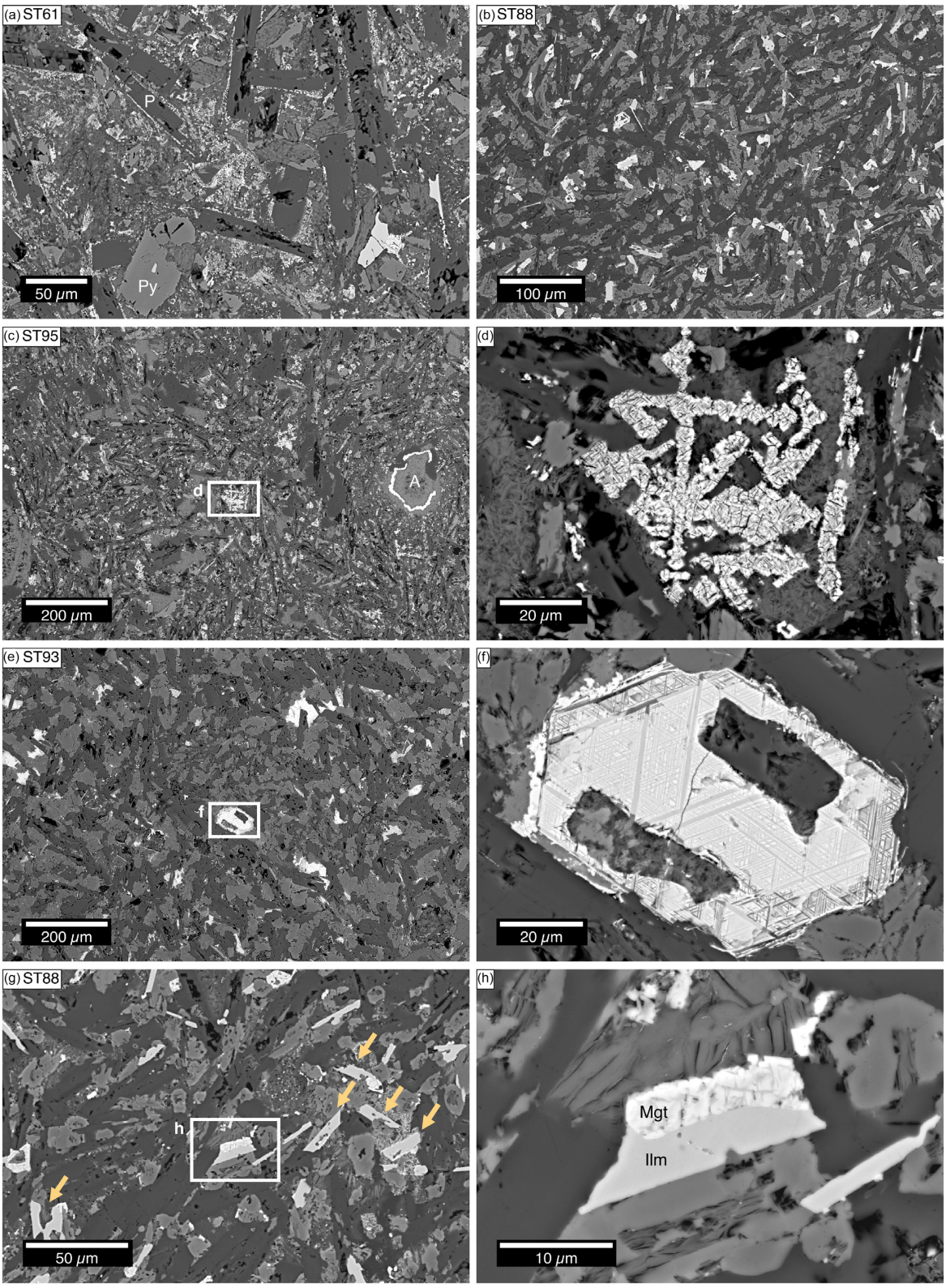

Figure 2. SEM images of oxide microstructures in CZ Stardalur basalts. The first two images (a, b) are overviews of oxide textures with maximal and minimal magnetite content. In (a) some plagioclase-P and pyroxene-Py phenocrysts are rimmed by magnetite. The next six images (c–h) show paired zooms of three examples of abundant ilmenite oxidation-exsolution lamellae in larger oxides. In (c) the rectangular box surrounds the magnetite grain enlarged in the left-hand column. Note in the far left part of the image is an amygdule (A) rimmed by hematite. In the enlarged image (d) the dendritic magnetite grain shows lamellae of ilmenite, and pleonaste needles. In (e) the magnetite shapes are unusual and commonly show edges with ragged textures. The enlarged image (f) shows abundant exsolution lamellae in the magnetite. The darker lamellae are titanite replacement of ilmenite.

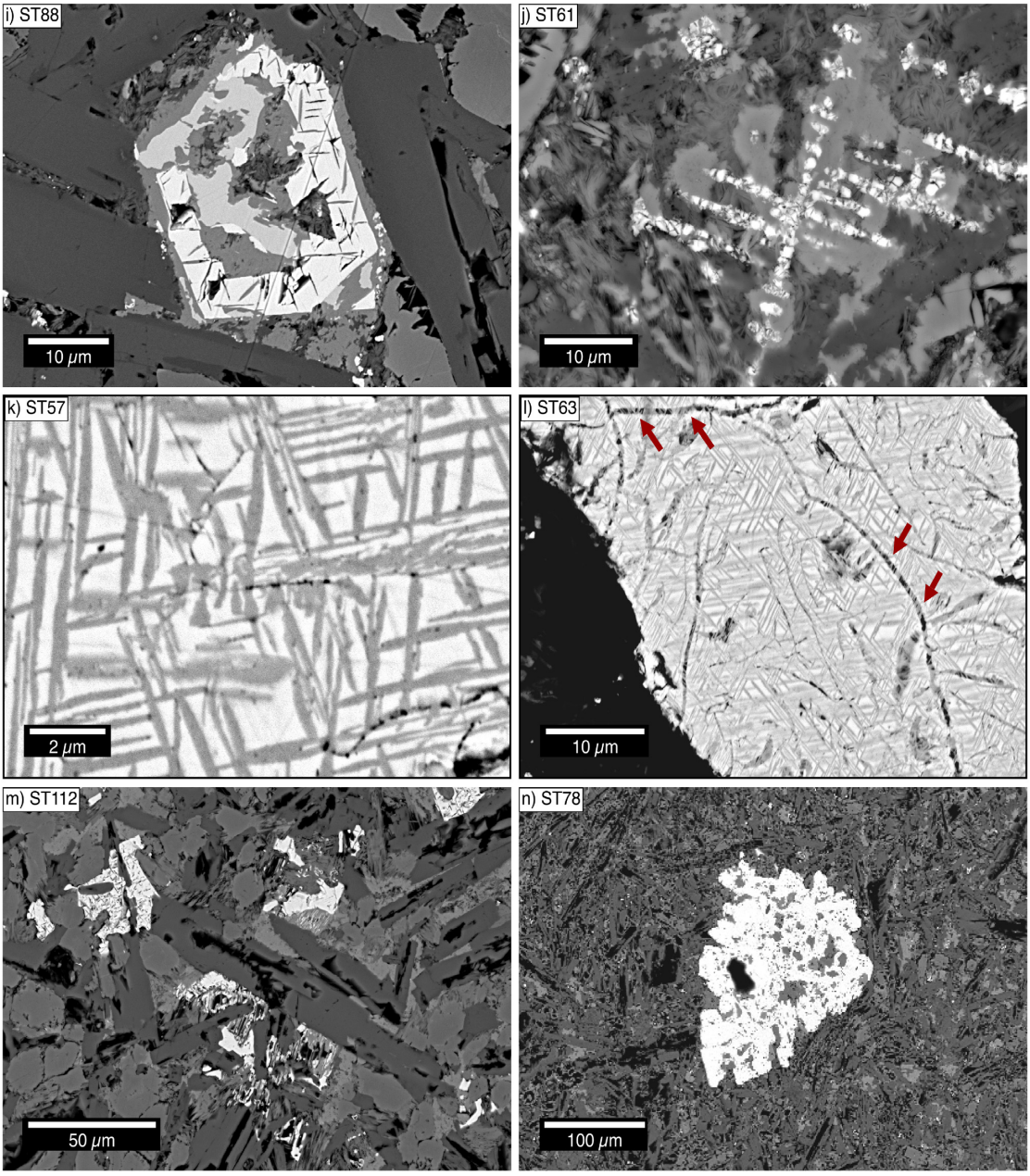

Figure 2. Continued.

matrix of numerous thin sections. Isolated matrix euhedral magnetite grains are usually $<1-2$ μm in width. Some plagioclase and/or clinopyroxene grains are partly rimmed by small magnetite grains (Fig. 2a), ranging from a few microns to <1 μm in width, and these typically lack microstructures, though ilmenite lamellae was observed in some of these magnetite grains. This rimming feature was more common around plagioclase than clinopyroxene, and only a minor amount of silicate grains contained magnetite rims, however the amount was variable between thins sections. In the more altered basalts magnetite grains with an anhedral morphology were observed in association with low temperature silicates such as chlorite. Plagioclase grains have variable amounts of alteration to sericite from <1 to >10 percent. Samples with the highest amount of alteration commonly contained more pyrite and chalcopyrite. Chlorite, smectite and hematite are typical weathering products from interstitial glass (Smith 1987) and these were observed in our study. Olivine phenocrysts, were not observed, however chlorite, and iddingsite, common replacements of olivine, produced during deuteric alteration were observed. Therefore, olivine may have been a primary phase in some of the CZ basalts. Quartz was present in the matrix of some samples. In numerous CZ basalts titanite ($CaTiO_5$) replaced some ilmenite lamellae in magnetite. Titanite lamellae in SEM images are much darker than the original ilmenite (Fig. 2f) due to the lower density of titanite compared to ilmenite.

Clusters of subhedral magnetite and sulfide grains up to >100 μm in size (Fig. 2n), and not containing microstructures, were associated with secondary alteration products. Hydrothermal fluids resulted in zeolite facies assemblages for many samples. Earlier workers observed chlorite alteration, but no epidote (SteinÞórsson & Sigvaldason 1971; Vahle *et al.* 2007), and we concur with these observations.

The estimated temperature for chlorite formation is from 200 to 250 °C. A study by Bleil *et al.* (1982) from a 1920-m-long core recovered from the lava pile of Eastern Iceland indicates that secondary formation of magnetite accompanies the appearance of epidote at temperatures of 250 °C and above (see Pálmason 2005). Primary oxides in the samples with which had evidence of hydrothermal fluids typically had significant alteration to both the magnetite and ilmenite grains (Figs 2m and n).

3.2 Oxides, microstructures and crack-like features in opaque grains

The most abundant microstructure observed in magnetite throughout the CZ was created by the abundant oxidation-exsolution of micron to submicron trellis (111) ilmenite lamellae in magnetite (Fig. 2k). Some large magnetite grains (>100 μm) contain a feature previously described as a 'curved crack-like feature' which was interpreted to be a sign of maghemitization (Vahle *et al.* 2007). In Fig. 2(l) red arrows mark these 'crack features' however, here it is clearly seen that these 'cracks' are crosscut by later ilmenite, or herzynite lamellae (Fig. 2l) an observation not reported earlier. In SEM backscatter images these 'crack features' are dark-grey to black in colour in contrast to the beige colour of the crosscutting ilmenite lamellae. In areas where there are several phases, these were too small for chemical analysis by EMP. This texture is reminiscent of a high temperature spinel–ilmenite–magnetite symplectite commonly observed at the border between a magnetite and ilmenite grains produced during cooling from high temperature (McEnroe *et al.* 2000) or ilmenite–spinel–pyrophanite intergrowths (McEnroe & Brown 2000). The cross-cutting relationship of the ilmenite and herzynite lamellae (Fig. 2l) indicate that this feature formed at high temperature, prior to oxy-exsolution of ilmenite lamellae from magnetite. We do not interpret this feature to solely indicate maghemite. Though maghemite may be present in small quantities, we did not observe it in our thin sections, except occasionally as a rim on magnetite. The dendritic and skeletal shapes commonly found in most thin sections and the microcrystalline matrix, glass inclusions in plagioclase and pyroxene phenocrysts, and hopper crystals all point to the basalts cooling rapidly. These shapes may indicate some crystal growth occurred in an undercooling environment.

EMP observations and analyses on magnetite phenocrysts confirm that our samples contain magnetite with abundant and very fine scale, ilmenite lamellae and spinel in the magnetite with a spacing commonly <1 μm. The dendritic, the skeletal, and most of the matrix magnetite grains were too small for EMP analyses. Though acceptable totals for magnetite analyses could not be obtained from our EMP measurements, analyses indicate minor substitutions in ilmenite and magnetite. The common elements other than Fe, were titanium, aluminium, chromium and manganese. Limited analyses on discrete ilmenite grains all had near end-member ilmenite compositions ($ilm_{98–100}$) with minor manganese substitution of up to 2.5 per cent. EMP analyses of pyroxene grains indicated these are clinopyroxene, and commonly a Ca-deficient clinopyroxene. Analyses of plagioclase compositions varied among flows, and ranged from $An_{41–64}$. Orthopyroxene was not found in any thin section. This observation questions the importance of magnetite formation by the oxidization of olivine to produce orthopyroxene + magnetite symplectite in our samples, as proposed by Vahle *et al.* (2007) as one cause of the high NRM intensities in CZ basalts.

There were three periods of glaciation while the Stardalur volcano was active. There is a large variation in alteration to plagioclase, ilmenite and glass in the different basalt flows, and the conditions of emplacement of basalts may play a role in alteration. For Ti and Al in basalts to be mobile the pH of the fluid must be low. Basalts erupting in some subglacial conditions have been documented to have acidic fluids (Jercinovic *et al.* 1990) and are more favourable to the mobility of Al and Ti (Gardner 1980; Crovisier *et al.* 1992). Samples with unaltered ilmenite (Fig. 2h) compared to those with titanite rims on magnetite grains, may be useful indicators of which lavas were extruded in a subglacial setting.

3.2.1 *Transmission electron microscopy*

For a more detailed characterization of the size and scale of the microstructures transmission electron microscopy (TEM) was used.

The results in Fig. 3, confirm that the magnetite and the ilmenite lamellae are intergrown in very fine spaced structure. The magnetite areas and ilmenite lamellae vary between 20 and 200 nm. Z-contrast STEM (Fig. 3b), shows that the phases, labelled A and B in Fig. 3, are alternating in average atomic number Z. Lattice imaging TEM demonstrate the layers are crystalline with common planes parallel to the interface between the two layers. In both magnetite and ilmenite small round (≈10 nm in diameter), amorphous inclusions were observed (arrows Figs 3b and c). These could be electron beam induced damage and are not further discussed here. The A-layers (magnetite) consist of mainly Fe and O, whereas the B-layers (ilmenite) contain Fe, Ti, O and minor amounts of Mn (arrow in Fig. 3g) based on EDX analysis (Figs 3d–g). The Cu peaks are due to stray radiation from the Cu half grid on which the FIB lamellae is placed. Atomic ratios Fe:Ti:O, as determined by Cliff-Lorimer method using Aztec, at the marked positions are at A 32:0:68 and at B 11:13:76 indicating magnetite and ilmenite, respectively. Using scanning precession electron diffraction, and crystal phase template matching, the two layers are also indexed as magnetite and ilmenite (Figs 3i–m). TEM observations indicate that the lamellae continue to be present at a smaller scale than is observed on the SEM. These measurements indicate that even the large magnetite grains contain small submicron areas of magnetite formed by dense amount of ilmenite lamellae. The EMP analyses which indicated the presence of manganese in the magnetite were likely overlap analyses of small submicron ilmenite lamellae in the magnetite, which here can be assigned to the ilmenite as a pyrophanite component ($MnTiO_3$) in the ilmenite-pyrophanite ($FeTiO_3$–$MnTiO_3$) solid solution.

3.3 Bulk sample densities

The Stardalur samples have a range in density values from 2300 to 2900 kg m^{-3} (Fig. 4), with an average and median value of 2600 kg m^{-3} with a standard deviation of ±200 kg m^{-3}. Sparks *et al.* (1980) calculated densities for a variety of basaltic compositions from Iceland and the mid Atlantic ridge. The average of our measurements are slightly lower than for basaltic rocks from eastern Iceland at 2700–2800 kg m^{-3}, and for the Atlantic mid- ocean ridge samples from 2600 to 2750 kg m^{-3} (Sparks *et al.* 1980). An increase in the amount of glass or in alteration will lower density values (Franzson *et al.* 2010). In the CZ samples the amount of vesicles and devitrified glass vary, comparing ST88 with 1 per cent vesicles to ST95, which has >5 per cent, densities of 2610 and 2420 kg m^{-3}, respectively. Overall, lower density samples in our collection contain more devitrified glass, vesicles and some are more altered.

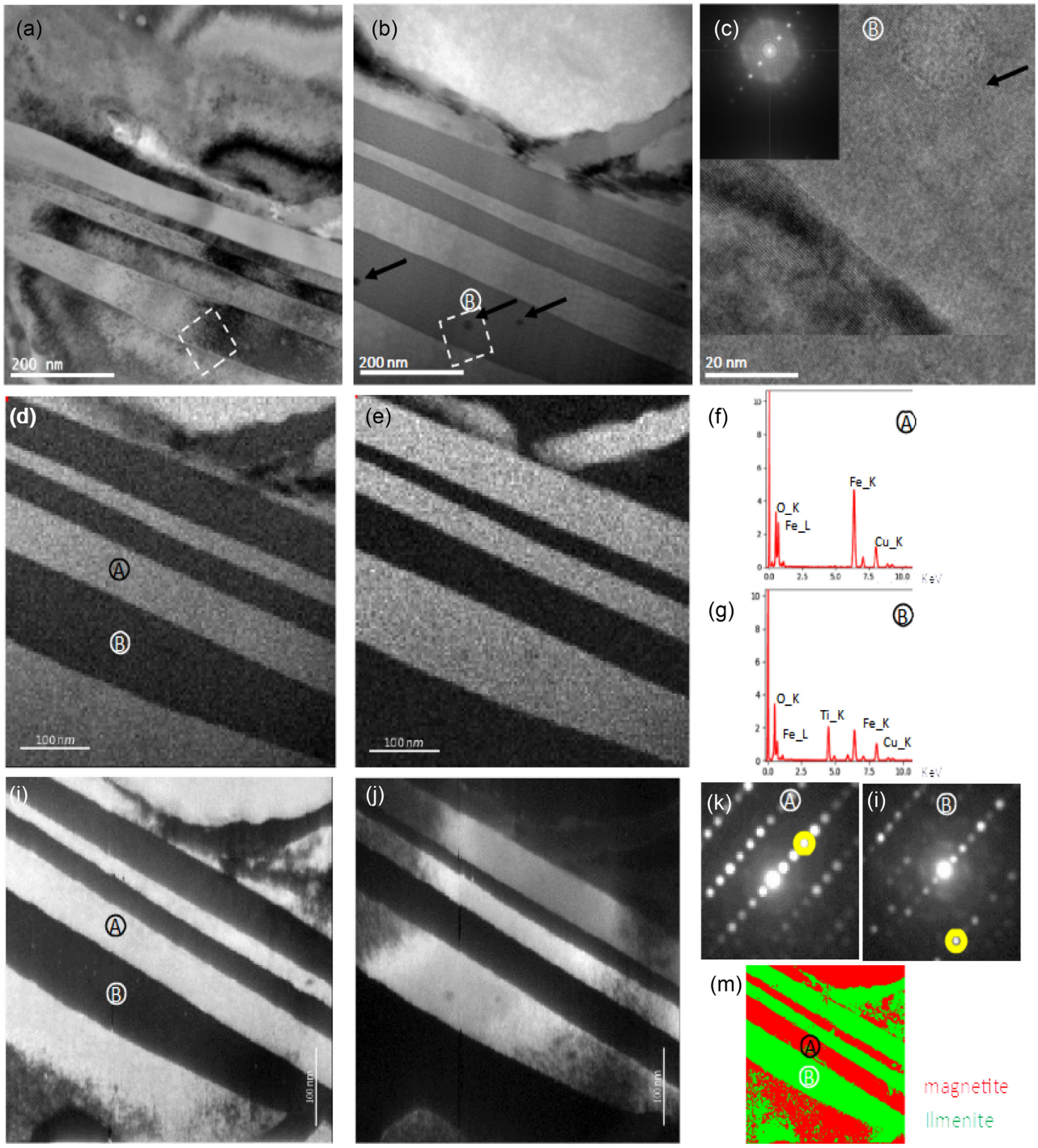

Figure 3. Sample ST57: (a) Bright-field TEM, (b) High-angle angular annular dark-field STEM. (c) High-resolution TEM of area marked in (a, b). Insert is fast Fourier transformation of the lattice image. Arrows mark inclusions or beam damage in (b, c). EDX analysis: (d) FeK_α and (e) TiL_α element maps together with (f, g) spectra at points marked A and B. (i, j) virtual dark-fields of reflections marked in point precession electron diffraction patterns (k, l). (m) Phase map, magnetite (red) and ilmenite (green).

3.4 Magnetic measurements

Early magnetic measurements on the Stardalur samples focused on susceptibility and NRM measurements to assess the origin of the aeromagnetic anomaly. Because the NRM was found to be the dominant contribution to this unusual anomaly, it became important to understand the rock magnetic properties of the mineral sources. Here, the first set of measurements focus on magnetic phase transitions to identify the magnetic minerals present in the samples, and their purity. These include low-temperature measurements of magnetic susceptibility which provide data for the presence of the Verwey transition, and high temperature measurements which determine the values and variability of the Curie temperatures, and also inform on the presence and abundance of additional magnetic phases. Detailed isothermal magnetic measurements at room

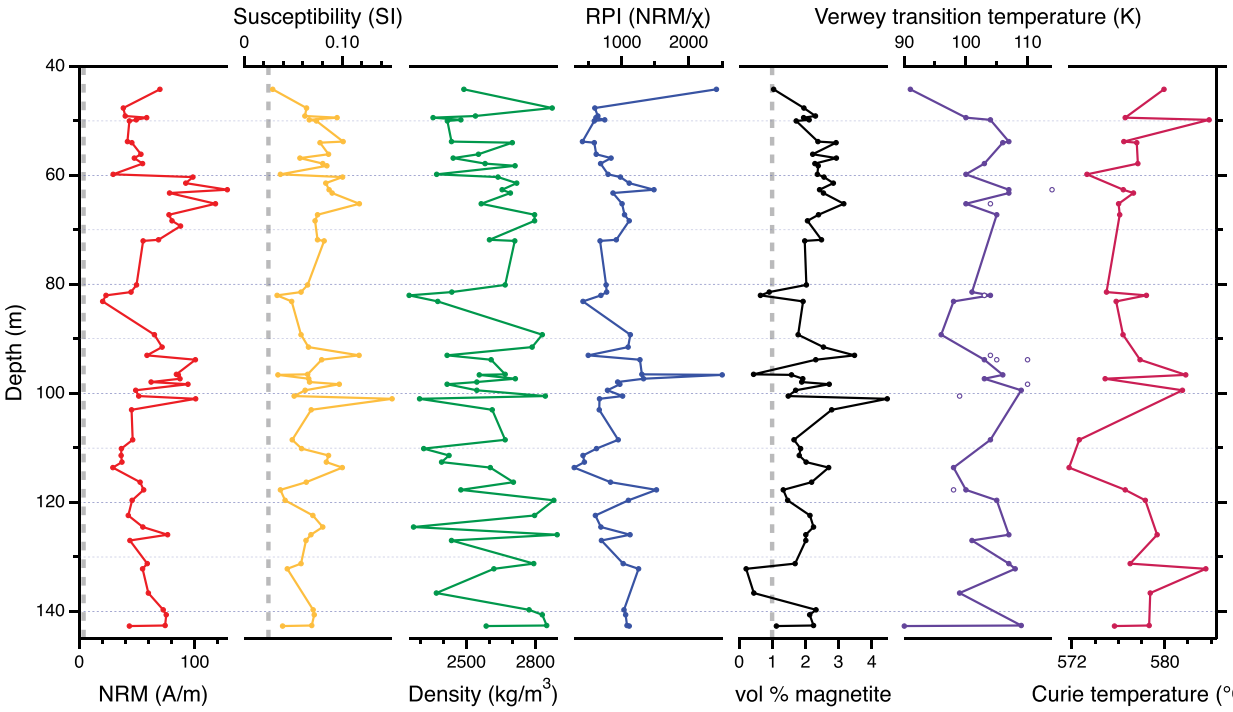

Figure 4. Downcore plots of NRM, χ (SI) and density for the critical zone of the Stardalur drill core. NRM/χ (blue) covaries with density (green), T_V (purple) and T_C (pink). Magnetite content (black) is estimated from saturation magnetization. Dashed grey lines indicate typical values of NRM, susceptibility, and magnetite content for Tertiary Icelandic basalts.

temperature probe the coercivity distribution and provide information about domain state, grain size, magnetic interaction or internal stress. Downcore measurement of magnetic and physical properties as a function of depth are provided in Fig. 4. The first three parameters are NRM, magnetic volume susceptibility χ (SI), and density. The ratio NRM/χ for homogeneous materials corresponds to a measure of relative palaeofield intensity (RPI). Here it broadly co-varies with other parameters such as density and T_V, T_C, indicating inhomogeneous mineralogy, grain size or remanence acquisition. The magnetite content (black line) was calculated from saturation magnetization measured on hysteresis loops. The last two curves in Fig. 4 display the measured temperatures T_V of the Verwey-transition and T_C of the Curie temperature. Dashed grey lines indicate typical values of NRM, susceptibility, and magnetite content for Tertiary Icelandic basalts.

Room temperature volume corrected susceptibility values ranged from 0.03 to 0.15 SI, with a mean and median of 0.07 SI, with a standard deviation of ±0.02 SI. Susceptibility values are commonly twice as high as the average susceptibility values of 0.025–0.035 SI for basalt flows in Iceland as reported by Kristjánsson (2013).

The four samples demagnetized by alternating fields had medium destructive fields (MDFs) between 16 and 25 mT with >90 per cent of magnetization removed by 50 mT. These values are very similar to the MDFs from 24 samples reported by Kristjánsson (2013) and Vahle *et al.* (2007), with values ranging from 14 to 34 mT.

There is a large range in the weight normalized saturation moments σ_s for the 59 samples, from 385 to 9331 mAm^2 kg^{-1}, reflecting varying concentration of magnetite from 0.2 to 4.5 per cent by volume. The median σ_s value is 3887 mAm^2 kg^{-1}, and the average is 3821 mAm^2 kg^{-1}. Magnetic remanent saturation moments (σ_{rs}) ranged from 61 to 2470 mAm$^{2\,kg^{-1}}$, with a median and mean of 653 and 664 mAm^2 kg^{-1}, respectively, yielding M_{rs}/M_s ratios of 1.68 and 0.174. and The median and average coercivity values (H_c) were nearly indistinguishable at 14.0 and 14.9 mT, as were the median and average coercivity of remanence values (H_{cr}) of 26.6 and 27.3 mT, respectively for the entire data set yielding H_c/H_{cr} ratios of 1.86 and 1.83, respectively.

3.4.1 *Hysteresis measurements and domain state*

There are several standard hysteresis parameters to study domain state in magnetite dominated rocks. The best known are the Néel plot of M_{rs}/M_s versus H_c (Néel 1955) and the Day plot of M_{rs}/M_s versus H_{cr}/H_c (Day *et al.* 1977). In the Néel plot in Fig. 5(a) the Stardalur samples lie on, or above, the average trend for magnetite (Hodych 1996), but note that most of the individual samples with comparable H_c in Hodych (1996) also lie above this trend line. The original trend plotted by Néel (1955, Fig. 6) uses data for 'eruptive rocks' and lies clearly above the Stardalur data which almost all plot in a narrow region with 10 mT$<H_c<$ 20 mT and 0.1 $< M_{rs}/M_s <$ 0.25.

All CZ basalts with NRM > 70 A m^{-1} have higher coercivities with H_c > 12 mT and M_{rs}/M_s > 0.12. Samples with 'low' NRMs <40 A m^{-1}, cover the entire range in coercivities, with a tendency towards lower values. In comparison to micromagnetic data of Nikolaisen *et al.* (2020), the data indicate a very narrow PSD H_c distribution in CZ basalts, possibly with slightly increased squareness, especially in samples with highest NRM.

Like the Néel plot, also the Day plot in Fig. 5(b) indicates a narrow domain state distribution of the Stardalur samples in the region of smaller PSD particles. Only ST36 shows distinct SD behaviour.

Constructing the Day plot requires to know H_{cr}, the absolute field at the zero of the backfield curve. The backfield curves contain much more detailed information, because its derivative can be interpreted as a distribution of microcoercivities in the sample. A detailed plot of the quantiles of these distributions is provided in Fig. S1.

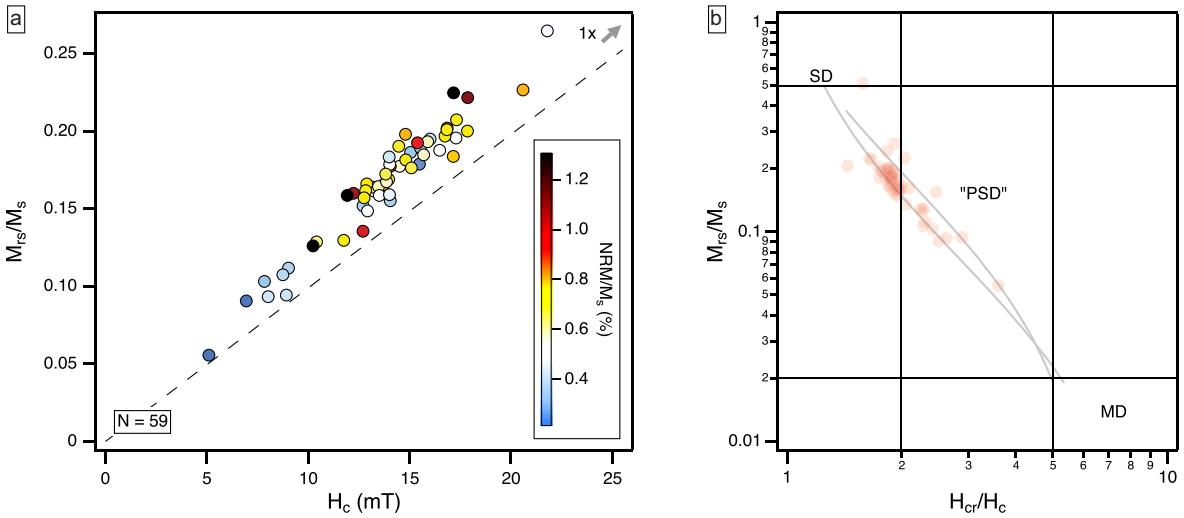

Figure 5. (a) Néel plot of M_{rs}/M_s versus H_c for the Stardalur samples, coloured by NRM efficiency. Dashed line is magnetite trend calculated by Hodych (1996). (b) Day *et al.* (1977) plot for same data set. Each disk has transparency 0.1, such that more intense colours reflect higher data density. Grey lines are SD–MD mixing lines calculated by Dunlop (2002) using alternative assumed MD properties.

4 THE STARDALUR EFFICIENCY ENIGMA

Here we encounter the difficulty in explaining the nature of the mineral source of the Stardalur anomaly by classical rock magnetism. Kristjánsson (2013, and references therein) has conclusively shown that the anomaly is controlled by the remanent magnetization which is carried by magnetite. Overall this magnetite requires a more efficient NRM acquisition process than thermoremanent magnetization. The underlying problem, is that no currently known natural process can explain this observed efficiency.

4.1 Decomposing the unusual NRM of Stardalur

In comparison to average Icelandic basalts (AIB) with a mean NRM of 4 A m^{-1}, the median NRM of 55 A m^{-1} at Stardalur is a factor $\Phi = 13$ times higher. Because the induced contribution to the Stardalur aeromagnetic anomaly at most is 12 per cent, the NRM clearly is the decisive factor to explain its unusual magnetization. In his review of the research on the Stardalur anomaly, Kristjánsson (2013) concluded that the unusual magnitude of the NRM which results in the large positive magnetic anomaly is due to a 'combination of circumstances (such as high magnetite content, high oxidation state, and strong ambient field) rather than to some unique phenomenon', such that none of them alone is sufficient to explain the full NRM enhancement compared to typical young basalts.

Here, we try to study systematically, and quantitatively, which processes, and properties, contribute to the anomalously high NRM values. To this end it is useful to decompose the NRM by several tautological relations. The first links the NRM to the magnetite concentration $c_{\rm Mt}$ and the constant room temperature saturation magnetization of bulk magnetite $M_s({\rm Mt}) = 480$ kA m^{-1} via

$$\frac{\rm NRM}{M_s({\rm Mt})} = \frac{M_s}{M_s({\rm Mt})}\frac{\rm NRM}{M_s} = c_{\rm Mt}\frac{\rm NRM}{M_s}, \qquad (1)$$

where M_s is the measured saturation magnetization of the sample. This relation assumes that the NRM is carried exclusively by magnetite, which will be discussed below. The ratio NRM/M_s denotes the fraction of the available *saturation* magnetization that is present as NRM. In contrast, NRM/M_{rs} is the fraction of the available maximal *remanent* magnetization that is present as NRM in the sample. For the Stardalur samples the relation between NRM/M_s and domain state as represented by M_{rs}/M_s is plotted in Fig. 6. NRM/M_s can be linked and decomposed by a sequence of additional tautological relations

$$\frac{\rm NRM}{M_s} = \frac{M_{rs}}{M_s}\frac{\rm NRM}{M_{rs}} = \frac{M_{rs}}{M_s}\frac{\rm NRM}{\rm TRM}\frac{\rm TRM}{M_{rs}} = \frac{M_{rs}}{M_s}\frac{\chi_{\rm NRM}}{\chi_{\rm TRM}}\frac{H_E}{H_0}\frac{\rm TRM}{M_{rs}}. \qquad (2)$$

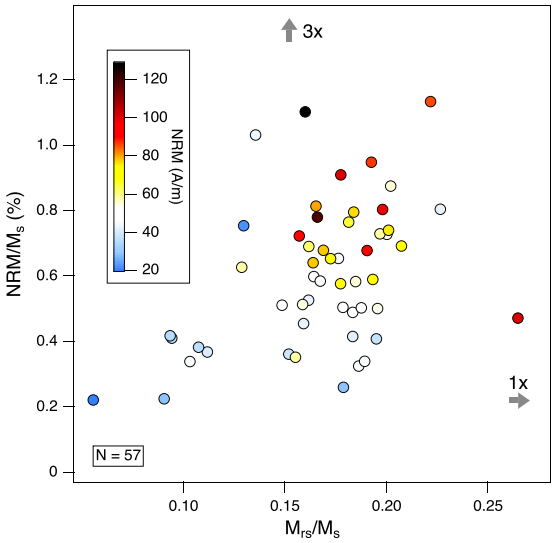

Figure 6. A plot of NRM efficiency NRM/M_s versus M_{rs}/M_s for CZ basalts indicates a trend towards higher efficiency for larger M_{rs}/M_s, which is commonly connected with smaller grain size. Symbol colours denote bulk NRM. Samples with $M_{rs}/M_s < 0.12$ have NRM <50 A m^{-1} and NRM efficiencies below ≈0.4 per cent. Within the region $0.12 < M_{rs}/M_s < 0.24$ no trend is visible except for a high NRM is commonly associated with higher NRM efficiency. This result implies that within this region the generally high NRM efficiency is controlled by additional factors not represented in this plot.

Here the laboratory TRM is acquired in the field H_0. The susceptibilities of remanence acquisition are $\chi_{\mathrm{TRM}} = \mathrm{TRM}/H_0$ and $\chi_{\mathrm{NRM}} = \mathrm{NRM}/H_E$, where H_E is the unknown external field in which the NRM has been acquired.

By introducing the above tautological relations we separated the problem of explaining the enhancement factor $\Phi = 13$ by which the Stardalur median NRM is larger than the average NRM of AIB into five independent contributions:

$$c_{\mathrm{Mt}},\ \frac{H_E}{H_0},\ \frac{M_{rs}}{M_s},\ \frac{\mathrm{TRM}}{M_{rs}},\ \frac{\chi_{\mathrm{NRM}}}{\chi_{\mathrm{TRM}}}. \tag{3}$$

In the following we analyse each contribution in this list, and attempt to estimate its magnitude.

4.2 Magnetite concentration

In the first step we discuss the validity of the assumption that the dominant magnetic mineral is magnetite, and try to estimate its concentration c_{Mt} in relation to AIB. Based on 17 chemical analyses reported on the Stardalur drill core the average total Fe content is 11 wt per cent (Steinþórsson & Sigvaldason 1971), a value considered to be slightly enriched for a typical basalt. However this value is well within the range of other basalts from the Reykjanes Peninsula (Jakobsson 1972). A geochemical study on younger basalts ≈ 4000 yr B.P. from lava shields and fissure eruptions within the Western Volcanic Zone (WVZ) in Iceland (Eason & Sinton 2009), report Fe content, percent of silicate phenocrysts, vesicles, and modal mineralogy from basaltic lavas. The Stardalur samples are well within the geochemical and mineralogical ranges reported for the WVZ lavas. There appears to be no major differences in silicate mineralogy of the Stardalur basalts from other similar tholeiitic basalts in the region.

4.2.1 Evidence from T_C and T_V data

Plotted in Fig. 7(a) are SIRM warming curves of 6 samples with a range in NRM from 23 to 128 A m^{-1} and NRM/M_s efficiencies of 0.35–1.1 per cent, and magnetic susceptibility measurements on warming of sister samples. All Stardalur samples show a clear Verwey transition (Walz 2002, and references therein) where more than 40 per cent of the LT remanence is lost over a relatively narrow temperature interval between 90 and 120 K. Magnetic susceptibility rapidly increases over a similar temperature range. The presence of a Verwey transition indicates magnetite is the dominant magnetic carrier in these samples.

The curves resemble data for crushed magnetite sized 399 μm (Dunlop & Özdemir 2018, Fig. 6), although the transition is smoothed and shifted to lower T_{V} values, indicating some degree of non-stoichiometry. The literature value for the Verwey transition is ≈125 *K*, however bulk oxidation beyond 4 per cent entirely suppresses it and leads to RT remanence fractions >50 per cent, while surface oxidation is indicated by a remanence drop of about 40 per cent over the temperature range 10–50 K (Özdemir & Dunlop 2010). Samples ST116 and ST57, which exhibit high NRM efficiencies of 0.88 and 1.1 per cent, respectively, are likely affected by some surface oxidation as shown by the remanence decreases of 10–20 per cent between 10–50 K. However, another sample exhibiting a high NRM efficiency of 0.91 per cent, ST88, shows no sharp magnetization decrease until it is warmed to 100 K.

A robust method for the calculation of the Verwey transition temperature using remanence data was described by Liu *et al.* (2004),

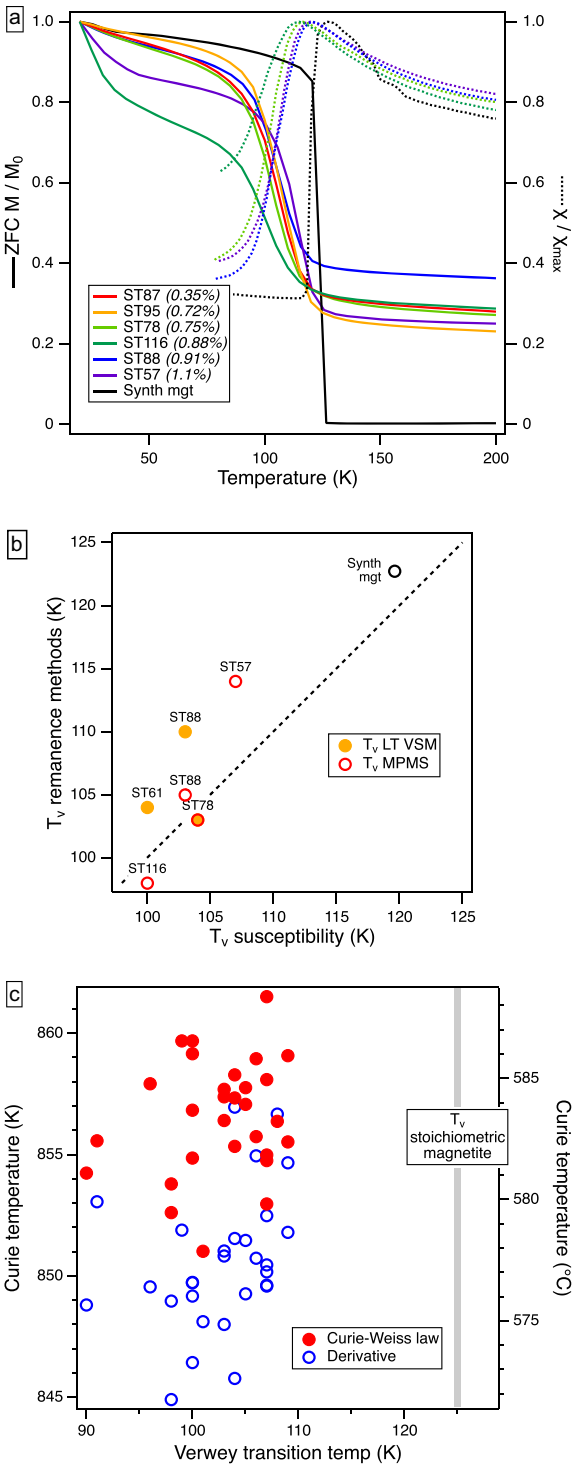

Figure 7. (a) Normalized SIRM warming curves for 6 Stardalur samples, compared to a polycrystalline MD synthetic magnetite. On right axis, normalized magnetic susceptibility of sister samples. Italized values in annotation indicate NRM efficiency NRM/M_s as percentage. (b) Comparison of values for Verwey transition temperature calculated from remanence data processed after Liu *et al.* (2004) and numerical derivative of susceptibility data. (c) Relation between T_{V} and T_{C} for the Stardalur samples. T_{C} was calculated from the same data using two alternative methods: the extrapolation of linear behaviour above T_{C} predicted by the Curie–Weiss law, and by estimating the inflection point from the numerical derivative of the susceptibility data to obtain the point of steepest descent.

however a physically justified technique for doing the same with magnetic susceptibility data is lacking. An empirical approach is to calculate the numerical derivative of the data and select the point of steepest ascent as the transition temperature. Fig. 7(b) compares the Verwey transition temperatures obtained using these two data types, including remanence data acquired on two instruments, the MPMS and a cryogenic VSM. Despite different underlying physical mechanisms, the variation between methods is similar to that which can likely be attributed to different specimens or different instrumentation as shown by sample ST88, which yielded a temperature difference of 6 K between remanence measurements acquired on two specimens measured on the MPMS and the low-T VSM.

Fig. 7(c) collects Curie temperatures T_C and Verwey temperatures T_V calculated from magnetic susceptibility measurements of 29 samples from the Stardalur drillcore. Two different methods to estimate T_C from $\chi(T)$. The first (red circles in Fig. 7) linearly extrapolates $1/\chi(T)$ for $T > T_C$ to $1/\chi(T_C) = 0$ and is known to lead to slightly too high estimates of T_C (e.g. Kneller 1962). The second method determines the inflection point in the slope of $\chi(T)$ as estimate of T_C (blue circles in Fig. 7). In a natural sample, where each magnetite particle has its own T_C and the bulk measurement represents a heterogeneous mixture of T_C values, the first method focuses stronger on an upper limit of the T_C distribution, whilst the second method rather represents an average of the T_C values in the sample (Petrovský & Kapička 2006; Fabian *et al.* 2013). T_V was estimated using the derivative method described above.

The data provide clear evidence that magnetite is the dominant ferrimagnetic mineral in all samples. Curie and Verwey temperatures are slightly correlated, in that higher T_C values close to the literature Curie temperature range of 578–583 °C for pure bulk magnetite correlate with higher T_V closer to the literature value of 125 K for pure bulk magnetite. Few T_C values in Fig. 7(c) deviate more than 10° from the literature value of 853 K (580 °C). Most of the Stardalur T_V values lie between 95 and 110 K, which coincides with an under-represented range of T_V values, though not uncommon for igneous basalts (Jackson & Moskowitz 2020). The T_C values excludes >2 per cent admixture of impurities and especially of Ti, or >1 per cent oxidation or vacancy concentration (Bowles *et al.* 2019). Reasons for a decrease in T_V in this range include extremely small particle size <20 nm (Lee *et al.* 2015), or extremely high stress >1 GPa (Coe *et al.* 2012) or a quantitatively fitting combination of several of the above effects.

4.3 Magnetite composition, grain size and oxidation exsolution

4.3.1 Magnetite composition

Shown earlier, the density of ilmenite lamellae, and minor spinel needles and blades in the CZ samples is very high. Coupled with the knowledge of high Curie temperatures, and presence of Verwey transitions in all measured samples implies that the chemical components other than iron in the original solid solution diffused to form the ilmenite lamellae and spinel resulting the near end-member composition of the host magnetite. Generally, our EMP analysis could not accurately determine the magnetite compositions because the EMP beam size of 1 μm is larger than the analysed magnetite grains, or compartmental magnetite sizes resulting in overlap analyses of the magnetite with lamellae. Yet, these analyses at least provide an upper limit of the Ti substitution of at most of 1–2 per cent remaining in some magnetite grains. TEM analyses in Fig. 3 at a finer scale provide evidence that in the regions which are subdivided into fine lamellae, the magnetite areas consist of Fe and O, whereas the ilmenite lamellae contain a small amount of manganese (Mn) in addition to Fe, Ti and O. The Mn is a pyrophanite component ($MnTiO_3$) in ilmenite. From our data on the CZ samples we suggest a maximum of 1–2 per cent substitution of Ti, or other contaminants for Fe is indicated by the very narrow T_C range close to 580 °C, which is supported by the clearly defined Verwey transitions above 100–110 K. If nanoscale lamellae thicknesses, as observed in the TEM images, are abundant in the CZ basalts, a part of the T_C spread must even be assigned to a grain size induced decrease of T_C (Shcherbakov *et al.* 2012; Penny *et al.* 2019).

4.3.2 Evidence from Mössbauer studies

Earlier Mössbauer studies on 28 samples from the Stardalur drill core (Helgason *et al.* 1990; SteinÞórsson *et al.* 1992) concluded that in samples from the CZ between 45 and 170 m the magnetite was generally found in a very pure state. Most samples had a B/A-ratio near 2/1 which is a hallmark of stoichiometric magnetite. X-ray diffraction measurements indicated that the magnetite did not contain titanium, and was not oxidized. Later Mössbauer studies of Gunnlaugsson *et al.* (2004, 2006) also confirmed that the magnetite is very pure, and proposed a mechanism for the formation of pure secondary magnetite by an exsolution mechanism from olivine during cooling. In the samples used for this study, we did not observe olivine in thin sections, however it may have been subsequently altered after, or during emplacement. Iddingsite and chlorite, common alteration products of olivine, were observed in our thin sections. The Mössbauer data support our determination that the magnetite in the CZ is almost of pure end-member composition. We note that in the upper part of the Stardalur drillcore, above the CZ, at depths <41 m, Mössbauer studies have documented maghemitization (Helgason *et al.* 1990; SteinÞórsson *et al.* 1992).

4.3.3 Magnetite concentration in Stardalur versus AIB

Having confirmed that the dominant magnetic mineral is magnetite, there are two ways to magnetically estimate the concentration c_{Mt} of magnetite. The first is to use a calibration factor $f = 0.0347$ to estimate the magnetite concentration in terms of MS as $c_{Mt} \approx \chi/f$ (Balsley & Buddington 1958; Clark 1997). Because of the ease of MS measurements this estimation is commonly reported in literature. A more precise measurement is performed on a smaller specimen size than that used for susceptibility measurements. It is based on the relation used in eq. (1) which is extended to

$$c_{Mt} = \frac{M_s}{M_s(\mathrm{Mt})} = \frac{\sigma_s\,\rho}{M_s(\mathrm{Mt})}, \tag{4}$$

where σ_s is the weight normalized saturation moment in units of $Am^2\,kg^{-1}$, and ρ the density of the sample.

The magnetite concentration c_{Mt} as determined from magnetic susceptibility in Stardalur basalts (Fig. 4) is at most 3–4 per cent. The calculated mean and median concentration is 2.1 and 1.9 per cent, respectively. The magnetite concentration c_{Mt} as determined from magnetic saturation ranges from 0.12 to 5.1 per cent, with a mean and median concentration of 2.1 per cent. Though the magnetite concentration calculation from σ_s and ρ should be more accurate, it may be less representative due to the smaller specimen size used in the measurement. However, we consider an average magnetite concentration of $c_{Mt} = 2.1$ per cent overall to be representative for

the CZ basalts. This concentration is between 1 and 2 per cent for typical tholeiitic basalts, and in AIB. Therefore, we assume that an increased c_{Mt} at most contributes a factor 2 to Φ.

4.4 Geomagnetic field intensity during NRM acquisition

Here we evaluate the contribution of the factor H_E/H_0 to Φ which requires one to estimate the intensity of the geomagnetic field during the emplacement of the Stardalur basalts.

The Stardalur basalts formed over a time interval of at least 100 ka in a normal period of the Matuyama chron, and radiometric ages of 1.8 Ma of correlative lavas suggest that they were emplaced during the Olduvai subchron (Friðleifsson & Kristjánsson 1972). Rocks of Matuyama age are the likely source of the wide negative anomaly lineation surrounding Stardalur. If the localized positive magnetic anomaly at Stardalur is due to rocks of comparable age as the acidic hyaloclastite, then these rocks date from the Reunion or Olduvai subchrons at 2.1 and 1.9–1.8 Myr, respectively.

Palaeointensity studies of Icelandic basalts do not indicate an unusually high field intensity during the Olduvai subchron, such that high geomagnetic field intensity can at best account for a 20 per cent increase with respect to AIB. Palaeointensity studies which included samples from the the Esja Complex do not show an anomalous high field (Goguitchaichvili *et al.* 1999) for the time period Stardalur lavas were emplaced. A palaeointensity study from Icelandic samples covering a longer time interval (0–3.3 Ma) also does not support an anomalous high field values (Cromwell *et al.* 2015). Earlier proposals of an unusually high geomagnetic field during the emplacement of the Stardalur basalts (Gunnlaugsson *et al.* 2006; Kristjánsson 2013) are not backed by independent data, and were simply suggested as an explanation for the high NRM values of the Stardalur samples. A geomagnetic field value required to explain the Stardalur NRMs would need to be at least three to four times higher than the average field intensity. In view of the existing field data for the period in question this appears extremely unlikely, and other factors that could result in a significant increase the NRM should be considered. Here, we assume that the contribution of H_E/H_0 to Φ is most likely ≤ 1.

4.5 Domain state and magnetic particle size

The third contribution to Φ in the list of factors (3) comes from the domain state parameter M_{rs}/M_s. Estimations of domain state rely on isothermal magnetization data from hysteresis loops, backfield curves, and FORC diagrams or Preisach maps. FORC diagrams of Stardalur samples are remarkably consistent and do not show a strong correlation between high remanence efficiency and the presence of any particular domain state. The FORC diagrams presented in Figs 8(a)–(c) are from samples exhibiting low remanence efficiency, while those presented in Figs 8(d)–(f) are associated with efficiencies in the top decile of all Stardalur samples. Figs 8(a), (d) and (e) show a peak offset by $\approx$20 mT from the origin along the B_c axis, with lobes extending along the axis and vertically in the positive and negative B_u directions. The offset peak and tri-lobate geometry have been attributed to vortex or multivortex states (Lascu *et al.* 2018), carried by particles with diameters $0.3 < d < 1.7$ μm (Muxworthy & Dunlop 2002). This domain state is dominant in most samples from Stardalur, regardless of remanence efficiency.

Signatures of other domain states are observed in a limited number of Stardalur FORC diagrams, but their presence is not sufficient to explain the samples with exceptional remanence efficiency. The FORC diagram for sample ST80 (Fig. 8b) displays contours along the vertical axis which are indicative of multidomain behaviour (Pike *et al.* 2001), which may be the explanation for this samples relatively poor remanence efficiency. Samples that contain clear single-domain signatures, however, are not always associated with high efficiency. ST87 (Fig. 8) is the sole FORC distribution in this data set that has a clear central ridge, diagnostic of non-interacting SD particles. However, the remanence efficiency of ST87 is not high for this sample set. By contrast, the FORC diagram of highly efficient ST36 (Fig. 8) has a region of negative signal along the vertical axis for $-120 < B_u < 0$ mT, which results from SD behaviour (Newell 2005), but the central ridge spreads widely above and below the B_c axis, indicating strong magnetostatic interactions. These two samples indicate that the presence of SD particles is not the origin of the high remanence efficiency at Stardalur.

The hysteresis parameters for the CZ in the Néel plot of Fig. 5 belong to typical PSD domain states in magnetite, but nevertheless have slightly increased M_{rs}/M_s ratios in relation to H_c when compared to the linear trend described by Hodych (1996). Micromagnetic models of unstressed naturally shaped magnetite crystals (Nikolaisen *et al.* 2020) result in similarly increased M_{rs}/M_s ratios for single vortex and single domain particles, such that no unusual processes need to be claimed to explain the observed trend in Fig. 5. It rather appears to indicate a very sharply defined magnetic grain size distribution with main contributions from particles, or compartments with diameter below 400 nm. If the relatively low magnetocrystalline anisotropy of magnetite is additionally supported by stress anisotropy, the corresponding compartment size could be slightly larger, however, the fact that few samples have coercivities $H_c < 10$ mT excludes the presence of a significant fraction of unstressed magnetite compartments with size >500 nm. This is supported by FORC and Preisach maps on samples in Fig. 8 which do not indicate the presence of significant coercivity fractions outside the interval 10–100 mT, and rather support the presence of strongly interacting small compartments. For all samples the backfield spectra presented in Fig. A1 show an extremely homogeneous behaviour in the CZ proving that the diagrams are representative. The narrow coercivity distribution will be important in relation to the discussion of ilmenite lamellae in the Stardalur CZ, however, here, it is sufficient to note that the M_{rs}/M_s values have a narrow distribution between 0.15 and 0.25, with some lower values down to 0.1. These values are not especially high in comparison to typical AIB such that the contribution of M_{rs}/M_s to Φ should be at most a factor 1.5.

4.6 TRM efficiency

The next factor we consider in the list (3) is the efficiency TRM/M_{rs} for the acquisition of TRM, which in magnetite depends linearly on the small field H_0 during cooling, and is also grain size dependent. Yu (2006) collected data for synthetic and crushed magnetite, and showed that TRM/M_{rs} for $H_0 = 50$ μT decays from approximately 9 per cent for single-domain particles to 1 per cent and below for particles of about 1–10 μm diameter. The TRM efficiencies relative to M_s and M_{rs} of 10 Stardalur subsamples are plotted in Fig. 9 in comparison to the corresponding NRM efficiencies of the bulk samples. The observed efficiencies TRM/M_{rs} scatter between 0.2 and 3 per cent with a concentration around 1 per cent and only three samples have high TRM efficiency near 3 per cent, close to values for single domain ensembles. Interestingly, these SD-like samples are the only ones where NRM efficiency and TRM efficiency are

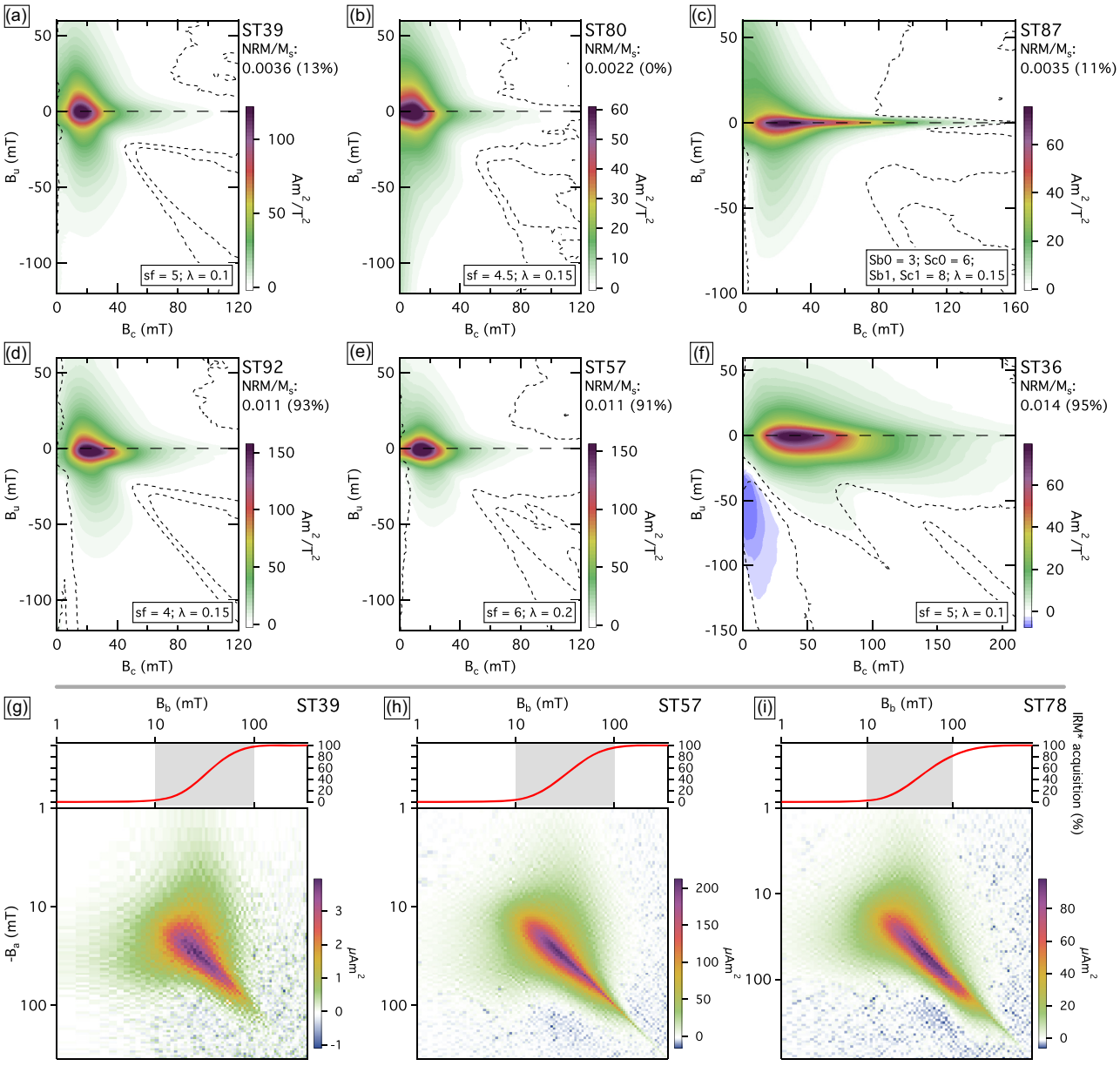

Figure 8. (a)–(f) First-order reversal curve diagrams of selected Stardalur samples, sorted by ascending NRM efficiency NRM/M_s (rank percentages of NRM efficiency of Stardalur samples). Fine dashed line is 95 per cent significance level and smoothing parameters for each graph shown in bottom right. (g)–(i) Non-linear Preisach maps of selected Stardalur samples.

almost equal, whereas for all other samples NRM efficiency is much higher. Overall the TRM efficiencies in the Stardalur CZ basalts are common for fine grained basalts measured by Yu (2006), Therefore here we assume the contribution of TRM/M_{rs} to Φ is also at most a factor 1.5, due to the fact that CZ basalts apparently contain more smaller PSD particles with increased efficiency than AIB.

4.7 NRM versus TRM susceptibility

To estimate the last factor in our list (3), in Fig. 9 the TRM efficiencies of the subsamples from the previous subsection are compared to the observed NRM efficiency for the corresponding whole samples. The most significant observation from this comparison is that the NRM efficiency is larger than TRM efficiency by a median factor of approximately 3, and up to a factor of 10. Notable exceptions are the samples with highest TRM efficiency close to 3 per cent, where NRM and TRM efficiencies are approximately equal. Collecting the estimations for the individual factors in eq. (3), we obtain

$$c_{\mathrm{Mt}} \to 2,\ \frac{H_E}{H_0} \to 1,\ \frac{M_{rs}}{M_s} \to 1.5,\ \frac{\mathrm{TRM}}{M_{rs}} \to 1.5,\ \frac{\chi_{\mathrm{NRM}}}{\chi_{\mathrm{TRM}}} \to 3. \quad (5)$$

In combination this leads to an estimate $\Phi_{est} = 2 \times 1 \times 1.5 \times 1.5 \times 3 = 13.5$ which is very close to the observed value. Note that for the first four factors, we were conservative in our estimates, and chose too high, rather than too low estimates, while for the last factor we used a median value.

While this estimation appears to be satisfactory, and to some extent confirms the conclusion of Kristjánsson (2013), the last factor poses a significant rock magnetic problem, because it implies that the NRM acquisition occurred by a substantially different—and more efficient—mechanism than the later laboratory TRM

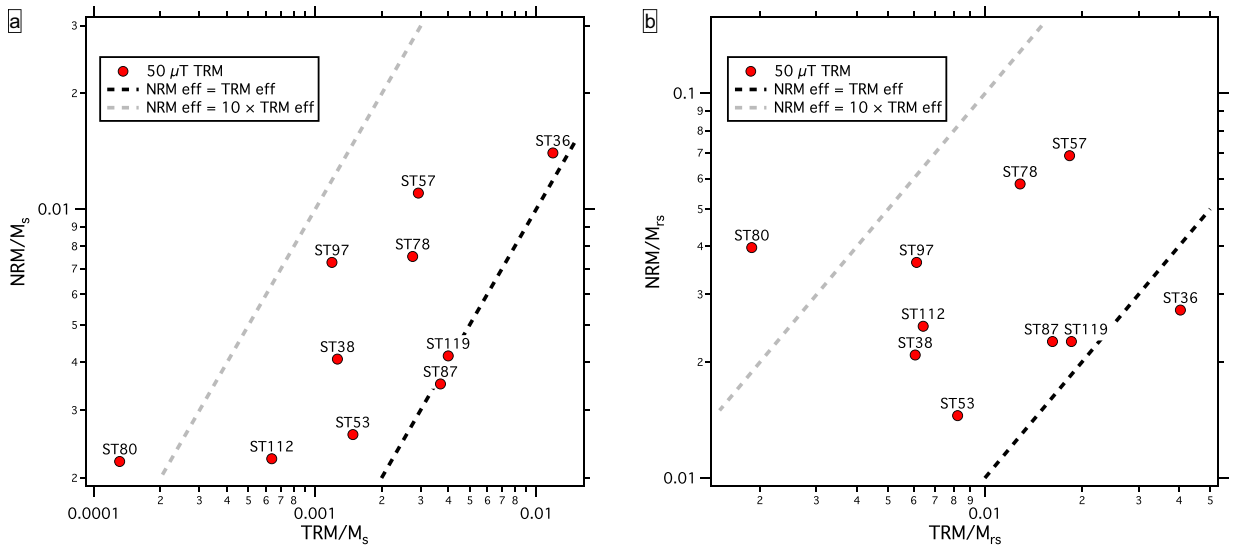

Figure 9. Left-hand panel (a) NRM efficiencies NRM/M_s and right-hand panel (b) NRM/M_{rs} versus the corresponding TRM efficiencies for a subset of the Stardalur samples. The thick dashed lines indicate equal efficiencies, which is achieved only for three samples with relatively high TRM efficiency. Samples with lower TRM efficiency, have NRM efficiencies which are on average at least three times higher, and some more than 10 times higher. This implies that the NRM cannot be explained by a simple TRM acquisition mechanism.

acquisition after reheating. If this can happen in typical basaltic magnetite—the best studied natural magnetic mineral—it implies that either we overlooked an extremely efficient mechanism of NRM acquisition, or that our rock magnetic theories of remanence acquisition are fundamentally flawed. The remaining part of this paper attempt to provide insight into possible mechanisms which could be related to a three times higher NRM efficiency as compared to later laboratory TRM acquisition.

5 POSSIBLE EXPLANATIONS OF THE UNUSUAL NRM EFFICIENCY

5.1 Evidence from high-temperature magnetic susceptibility data

The high-temperature magnetic susceptibility (HTMS) curves of CZ Stardalur basalts display an interesting feature that provides an independent rock magnetic parameter with positive correlation to the NRM efficiency NRM/M_s.

Fig. 10(a) illustrates that on heating the HTMS curves show varying degrees of a non-convex behaviour (green shading) between approximately 150 and 400 °C. The green area above the convex hull (black) in relation to the total area (blue+green) defines a non-convexity ratio $R_{nc}(150, 400)$ that lies between zero and 1, but typically is <3 per cent. Because $R_{NC}(150, 400)$ is uncorrelated to changes in T_V or T_C, it appears not to be linked to oxidation degree.

The plot of NRM/M_s versus $R_{nc}(150, 400)$ in Fig. 10(b) indicates that for $R_{nc}(150, 400)$ <3 per cent increased $R_{nc}(150, 400)$ is correlated with increased NRM efficiency, but it should be noted that also the samples with lowest $R_{nc}(150, 400)$ <0.3 per cent have already unusually high NRM values. Data from aged synthetic magnetite (black bottom marks) suggest that laboratory or natural surface oxidation is a potential source of $R_{nc}(150, 400)$. For Stardalur basalts the observed trend (blue line)—if due to oxidation—implies either that slightly oxidized samples acquire NRM more efficiently, or that highly efficient NRM carriers have a larger surface exposed to laboratory oxidation. Dendritic shapes which are a result of faster growth along energetically favourable crystallographic directions have large surface areas that could be more susceptible to oxidation during high-temperature experiments. That irreversible non-convexity $R_{nc}(150, 400)$ is an intrinsic property of magnetite is also demonstrated by the data of Dunlop (2014, Fig. 3a) for crushed, sized magnetites (red marks in Fig. 10b, Dunlop (2014) assigns its origin to lattice strain produced by crushing. In all synthetic samples $R_{nc}(150, 400)$ reflects processes at room temperature or during heating, be it strain or surface oxidation, and not previous high-temperature oxidation. In the CZ basalts $R_{nc}(150, 400)$ may indicate either frozen (non-annealed) lattice strain, or room-temperature oxidation due to a relatively large exposed surface area, and accordingly small grain size. In all the above cases, the T_V, T_C results strictly limit the amount of oxidation or impurity to less than 1–2 per cent. Hydrothermal fluids, or reheating are not required to create $R_{nc}(150, 400)$ <3 per cent, and more readily could be assigned to the samples with very high values of $R_{nc}(150, 400)$ which plot outside the range shown in Fig. 10(b). The correlation with NRM/M_s suggests that the corresponding process is related to the enigmatic overefficiency and thus must be able to modify the NRM and occurs below T_C. It appears that this unknown TCRM acquisition process synchronously generates low-temperature strain that could result in the unusually high NRM in the CZ basalts. Whether this process could be related to a magmatic history that includes undercooling, or if this process would lead to magnetite growth and textures that could result in an unusual high efficiency of NRM acquisition is yet to be determined.

5.2 TCRM acquisition as potential physical process

There are several physical mechanisms which could lead to unusual NRM acquisition. Most of these can be included under the terminology of thermochemical remanence acquisition (TCRM). Nearly

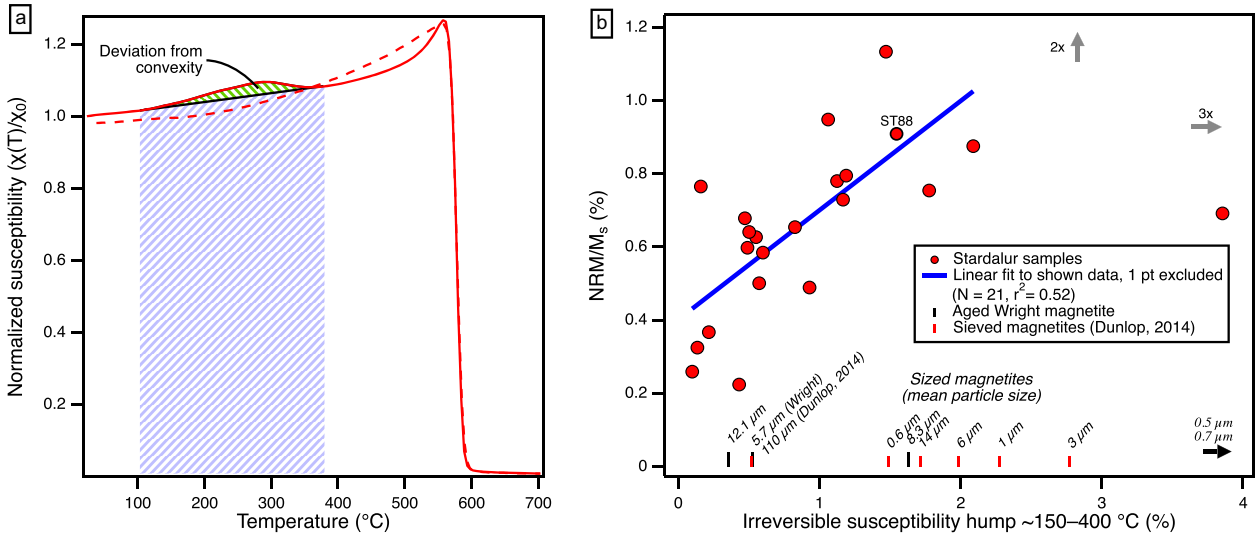

Figure 10. Left-hand panel (a) High-temperature magnetic susceptibility curves of CZ Stardalur basalts on heating show varying degrees of a non-convex behaviour (green shading) between approximately 150 and 400 °C. The green area above the convex hull (black) in relation to the total area (blue+green) defines a non-convexity ratio $R_{nc}(150, 400)$ between zero and 1. Solid red line is the heating curve of sample ST88, dashed red line is the cooling curve. Right-hand panel (b) NRM/M_s versus $R_{nc}(150, 400)$ for CZ Stardalur basalt (red circles). Black bottom marks provide $R_{nc}(150, 400)$ from aged synthetic magnetite. Red bottom marks are $R_{nc}(150, 400)$ values measured from Dunlop (2014, Fig. 3a) for crushed, sized magnetites.

all CRM or TCRM acquisition processes are theoretically, and experimentally found to be less efficient than TRM acquisition, which leads to an underestimation of the palaeofield intensity if these are interpreted as TRM (McClelland-Brown 1982; Draeger *et al.* 2006). Yamamoto *et al.* (2003) and Yamamoto (2006) postulated that ilmenite exsolution affects the TCRM acquisition process and can lead to palaeofield overestimation of up to 70 per cent. This could be related to an increase of the (un-)blocking temperature that occurs below the blocking temperature, at a later time in the cooling process (Fabian 2009). Fine scale exsolution below the magnetite T_C is a possible process leading to high NRM efficiency, but an efficiency of 300 per cent for this TCRM would still require a novel explanation. It is unclear whether the same processes which lead to palaeofield overestimation may also explain the uncommonly large NRM in Stardalur, or whether these only stabilize the acquired TRM beyond its original blocking temperature without notably effecting the NRM intensity.

Thermochemical remanence acquisition by ilmenite (oxy)-exsolution below magnetite T_C may increase χ_{NRM}. SEM observations confirm high abundances of fine-scale ilmenite exsolution in the magnetite grains of the CZ. Our SEM studies indicate that basalts from the CZ are unusual in that fine, and very fine scale oxy-exsolution is ubiquitous, and that it generates a very homogeneous and constrained distribution of magnetite compartment sizes in the approximate interquartile range of $\ll$500 nm. Our TEM observations indicate that this (oxy)-exsolution microtexture continues down to 50 nm. It is possible that this atypical and very dense exsolution microtexture may be related to the unusual NRM efficiency of the Stardalur basalts. Such fine-scale lamellae growth may occur below magnetite's T_C by diffusion of Ti. In this scenario a low-T_C titanomagnetite would decrease its Ti content by exsolution and acquire a remanence by continuously moving its chemical T_C boundary. It is conceivable that a changing diffusive chemical gradient during such a process leads to a 'slow' blocking transition which in turn leads to a much more efficient NRM acquisition, but to date this hypothesis is not supported by a quantitative theoretical model.

5.3 Hydrothermal alteration

Hydrothermal alteration has been put forward as a possible cause for the high NRM in CZ basalts (Vahle *et al.* 2007). Alteration at lower temperatures may change the grain size of the TRM carriers. As shown in Fig. 2(m) large parts of magnetite grains are destroyed by hydrothermal fluids. To increase the NRM efficiency by such a mechanism is theoretically possible, for example if the initial TRM was acquired by large SD grain sizes, which later are partly dissolved to a finer grain size distribution with equal magnetization but higher blocking temperature. Because such a process requires exact fine tuning between the original grain size distribution and partial hydrothermal dissolution it is not conceivable that it would homogeneously occur over the total volume and emplacement time interval of the CZ. Therefore we consider this mechanism as highly improbable.

Recently, Kanakiya *et al.* (2021) report a more than tenfold increase of NRM in combination with decreased magnetic susceptibility due to acid-sulfate hydrothermal alteration in lavas from the Whakaari Volcano, New Zealand. In their experiments they find that high NRM in altered samples is related to a high frequency-dependent magnetic susceptibility $\chi_{FD} \approx 8$ per cent in contrast to $\chi_{FD} < 2$ per cent in less altered, or unaltered samples, suggesting that the increased NRM is carried by an SP–SD phase of Fe–Ti particles. As possible mechanisms Kanakiya *et al.* (2021) consider (i) that the altered samples initially had an even higher NRM (ii) alteration removes a ferrimagnetic fraction that shielded the high NRM fraction and (iii) a new fraction of ferrimagnetic grains formed such that they enhanced the existing NRM. In case of (i) and (ii) the high NRM phases should have a substantially lower concentration of ferrimagnetic grains, and the question of how the residual phase acquired their highly efficient NRM remains the same. In case of (iii) the newly formed phase should be recognizable and abundant. In the Whakaari basalts it is not reported that the increase of NRM is related to a high NRM efficiency. The authors note that the fine grained Fe–Ti oxides in the basaltic glass are protected from alteration, and only the altered lava samples showed an increase in

magnetization, while the NRM in all tuff and breccia samples decreased. This implies that external factors related to a high field, or high NRM efficiency do not play a role. Therefore an additional chemical remanent magnetization (CRM) by grain growth is a feasible explanation for Whakaari. The conditions for alteration for the Whakaari samples are quite different from the Stardalur samples with higher hydrothermal temperatures, and more alteration to the silicates.

At Stardalur an additional phase is more difficult to put forward as a possible source of the high NRM. If it is separate from the primary ferrimagnetic phase, again the question arises why its NRM is much more efficient. This leaves the possibility that the newly formed magnetic phase is coupled to the initial NRM such as to enhance the predominant direction of remanent magnetization. However, there is no known mechanism that would enhance a previous NRM as to make it more efficient. Variable amounts of hydrothermal alteration is present in the Stardalur drillcore samples. Iron sulfides are more abundant in the heavily hydrothermally altered samples. These samples also have the lowest NRM intensities in the entire CZ data set. Samples ST78 and ST112 (Fig. 2) contained large amounts of alteration products, abundant pyrite and chalcopyrite, the magnetite grains were anhedral to subhedral, and few dendritic shaped magnetite grains were observed in the matrix. Secondary magnetite grains did not contain titanium, or any oxyexsolution lamellae. NRM values of the altered samples are in the lower quartile for Stardalur basalts. This contradicts the possibility that a newly formed magnetite phase carries the unusually effective NRM. This also excludes that the increased concentration of magnetite in hydrothermally altered regions may have caused the strong magnetic anomaly at the surface (Vahle *et al.* 2007).

In the Stardalur samples, as shown in Fig. 9 samples ST36, ST87, ST119 show that a more predominant SD phase leads to lower NRM efficiency. While at Whakaari the increased NRM is related to an SP-SD phase, this is not the case at Stardalur.

5.4 Magnetite–ilmenite interface magnetization?

An unexplored possible contribution to the NRM is from an interface moment. A few studies with rhombohedral-cubic intergrowths provide evidence of unusual magnetic properties, including high NRM and coercivity, possibly enhanced by magnetic coupling between the phases, along the common rhombohedral {0001} interface and {111} in the cubic oxide (see Robinson *et al.* 2016). It is not clear how common such strong interactions and magnetic superstates are in natural samples. In magnetite–ilmenite intergrowths the potential magnetic effects along the (111)–(001) magnetite ilmenite lamellar contacts were considered by (Robinson *et al.* 2016).

There are distortions between intergrowths of rhombohedral ilmenite and cubic magnetite. The magnetite parameters (Fleet 1984) of 'a' = 5.9369 Å, where magnetite layers have a repeat distance of 14.5424 Å compared with ilmenite a = 5.0885 Å and c = 14.0924 Å (Wechsler & Prewitt 1984), indicates magnetite–ilmenite strains of 0.8981 along 'a' and 1.0319 along 'c'. These strains in cubic-rhombohedral interfaces are significantly larger than strains between the rhombohedral oxides of hematite and ilmenite. As discussed by Robinson *et al.* (2016) the stretching of magnetite along 'a' limits lateral growth and the compression of magnetite along 'c' could also limit growth in that direction. The Fe–O–Fe bond angles are effected by the stretching along 'a' and compression along 'c', which could have an effect on magnetic interactions. Magnetostriction in these regions could influence bulk magnetic properties. Robinson *et al.* (2016) calculated a lamellar component for a magnetite–ilmenite interface which involves the positive moments of two contact layers minus the unbalanced negative moment of one conventional tetrahedral–octahedral layer. The net lamellar moment for one lamella is +53.5 μ_B compared to a ferrimagnetic moment of +48 μ_B for four layers of magnetite. This results in a large increase in the lamellar moment which is a consequence of the paramagnetic ilmenite Ti layer. The magnetite moment would be increased by adding groups of six layers between the magnetite layers, each set of six providing an additional +72 μ_B to the positive net moment. The concept that lamellar magnetism by Robinson *et al.* (2002) may occur where one of phases is a cubic oxide, in contrast to both rhombohedral phases, is explored by Robinson *et al.* (2016) in their fig. 16. Because magnetite already has such a high magnetic moment, this additional component may be overlooked, and would be significantly lower in magnetite grains with moderate amount of lamellae, or where lamellae have coarsened. Both examples limit the amount of interface area. Here, where very fine and dense lamellae are abundant, it is possible that a lamellar component could contribute to the NRM. If there is Fe^{2+}/Fe^{3+} charge ordering at the interface of the rhombohedral (ilmenite) and cubic oxide (magnetite) this, and related charge-balance matters could be explored further using bond-valence theory as was constructed for the ilmenite–hematite interface Robinson *et al.* (2006). Irrespective of the nature of the magnetite–ilmenite interface there is significant strain associated with this interface due to the different lattice parameters of the two phases. Dependent at which temperature the interface formed an interface magnetization could be acquired either as a TRM or TCRM. Interface related physical mechanisms for unusual efficiency of NRM acquisition have earlier been discussed by Fabian *et al.* (2008) and McCammon *et al.* (2009), for lamellar magnetism in the ilmenite–hematite system, and in titanohematite by McEnroe *et al.* (2001). In these cases the acquisition of NRM is considered to be synchronous with the formation of 1–100 nanometer sized lamellae.

5.5 Stress generated by oxidation–exsolutions

Stress generated by oxidation-exsolution (or exsolution 'sensu stricto') is a property that could influence NRM acquisition. The high density of ilmenite lamellae ubiquitous in the magnetite grains of the CZ not only leads to fine scale compartments, but also generates increased internal stress levels. Comparison of stress-free micromagnetic models with measured hysteresis loops provides magnetic indications for elevated internal stress (ter Maat *et al.* 2020). A physical model of stress and strain formation during oxyexsolution and exsolution processes, and especially for a qualitative understanding of its interaction with the magnetic blocking process presently does not exist, but a quantitative method of stress determination in magnetite is in development (Béguin & Fabian 2021). A quantitative model of the generation of stress during low-temperature oxidation of titanomagnetite (Fabian & Shcherbakov 2020) indicates that a non-linear vacancy diffusion process can generate excessive local stress up to 1 GPa, and maintains a high gradient in lattice spacing. If similar stress magnitudes can be generated and maintained by Ti diffusion during either oxidation-exsolution below magnetite's T_C, or exsolution once temperatures are below the solvus temperature. The proposed miscibility gaps based on phase equilibria experiments are by Lindsley (1981), who used natural samples and Vincent *et al.* (1957), using synthetic samples. The maximum consulate temperature is based on the experiments

of Lindsley which indicates 560 °C $< T_{consulate}$ which is below the T_C for pure magnetite 580 °C. A continuum of lamellae formation below magnetite's T_C could lead to complex TCRM acquisition mechanisms. If this is the case, then we require a better understanding of this mechanism.

5.5.1 From grain size to compartment size

Fine scale ilmenite lamellae occur in most magnetite particles subdividing them into substantially smaller magnetite cells. The strength of the magnetostatic interaction between these cells is controlled by the thickness of the intermediate ilmenite lamellae, and the number of subcells in the grain, which is related to its total volume. SEM images indicate that the extensive lamellae of ilmenite in the magnetite grains which range in size of 100 to <1 μm creates a very uniform grain size distribution in the submicron range. Minor amounts of magnetite with significant coarsening of the ilmenite lamellae are present in some samples. In addition, spinel as fine blebs or needles is observed in many magnetite grains. Very fine dendrites of magnetite are abundant in the matrix of the thins sections studied here, and these commonly have the microstructures created by the formation of ilmenite and spinel (oxy)exsolution. Room temperature magnetic hysteresis data of the Stardalur CZ basalts indicate the predominance of a constraint coercivity interval of 10–100 mT that is characteristic for SD-PSD magnetite. This is visible in the backfield curves in Fig. A1, which plots the percentiles of the remanence reversed from the initial value of M_{rs} to the final value of $-M_{rs}$ during the backfield measurements. The band between 20 and 90 per cent of reversed remanence lies between 10 and 100 mT. The only exception is the topmost sample ST36 where this range lies between 40 and 230 mT. First order reversal curves in Figs A8 and A9 further elucidate this behaviour in that these add to this confined B_c range the information that these coercivities typically are related to a substantial spread of up to 50 mT in the interaction field, which agrees with the microscopic observation of dense microtexture in the magnetite with closely spaced PSD sized compartments. The central ridge rarely extends beyond 100 mT and also shows a B_u spread of at least 10 mT. A more detailed analysis of these remanence features can be obtained using the non-linear Preisach maps in Fig. A7. The IRM acquisition curves calculated from the Preisach maps, again show the clear B_c confinement between 10 and 100 mT. Multidomain magnetite would contribute a significant fraction of lower B_c remanence. The amount of low coercivities would only be increased by the abundant magnetostatic interaction. Because the SEM images show a large fraction of magnetite minerals with sizes above 1 μm, the magnetic data support the observation that these large minerals contain fine scale ilmenite (oxy)-exsolution creating magnetite compartments in the PSD size with coercivities above 5–10 mT.

5.5.2 Undercooling

Observations such as skeletal magnetite and plagioclase crystals, melt inclusions in some phenocrysts and microtextures all point to undercooling [$\Delta T = T$(liquidus) $-T$(crystallization)] involved in the evolution of the lavas occurring close to their emplacement conditions. Rapid growth at moderate to high degrees of undercooling generates skeletal to dendritic crystals which commonly have disequilibrium compositions (Faure *et al.* 2003; Welsch *et al.* 2014; Shea *et al.* 2015; Salas *et al.* 2021). Bennett *et al.* (2019) provides a detailed evaluation of skeletal plagioclase crystals, and the significance of plagioclase textures in the physiochemical conditions and processes that control the plagioclase textures from mid ocean ridge basalts from the Gakkel Ridge. Clearly, rapid cooling of the lavas occurred which resulted in the very fine matrix rich in dendritic and skeletal magnetite grains, and abundant amount of glass in our samples. Undercooling could have provided the conditions for the formation of abundant and very fine ilmenite lamellae. However, a detailed geochemical study of the phenocrysts, in addition to the more morphological and textural observations of the CZ basalts is required to ascertain if undercooling conditions were part of the magmatic history of the CZ basalts.

6 CONCLUSIONS

Despite decades of magnetic studies, a full rock magnetic explanation of the origin of the Stardalur magnetic anomaly remains enigmatic. In the CZ basalts, magnetite is the primary source of the unusual 27 300 nT (above background) magnetic anomaly. The Stardalur CZ basalts encountered between 41 and 170 m depths, all have very high natural remanent magnetic intensities, with an average NRM of 61 A m^{-1}. In general the magnetite grains in the CZ behave like PSD particles common to many other basalts found world wide. What may be different with the CZ basalts is that magnetic properties indicate a narrow domain state distribution in the region of smaller PSD particles, with a focused magnetite grain size distribution of 100–400 nm, likely reflecting the magnetite compartment sizes between densely oxy-exsolved ilmenite lamellae, and to a lesser extent the exsolution of pleonaste. It is possible that this atypical, and very dense exsolution microtexture, may be related to the unusual NRM efficiency of the Stardalur basalt.

Here, we analysed several possible mechanism which could lead to high NRM, and concluded that the main issue is an unusually high efficiency of NRM acquisition in the magnetite grains, which is at least a factor of 3 higher than their expected TRM efficiency. Our argumentation is based on a synopsis of all available data, and new measurements of magnetically relevant properties of the CZ basalts. Earlier explanations for the NRM values, requires a palaeomagnetic field intensity during the emplacement of the CZ basalts to be significantly higher than for today's magnetic field. Palaeointensity studies on nearby Icelandic sites do not support this interpretation, and in fact provide contradictory evidence to this notion.

Using rock magnetic measurements and petrographic observations of the magnetite grains in CZ basalts we have investigated the nature of the NRM in the basalts, and only found one independent rock magnetic parameter [$R_{nc}(150, 400)$] which shows a weak positive correlation with NRM efficiency. This correlation supports the idea that the unusually efficient NRM acquisition is closely linked to the microstructure of abundant lamellae which, for example, could lead to increased strain at the interface of the ilmenite lamellae within the magnetite host. Though a physical mechanism that would explain the substantial increase in NRM efficiency due to such microstructural effects is still to be discovered.

ACKNOWLEDGMENTS

This paper is dedicated to Leo Kristjánsson whose interest in the mineralogy and magnetic properties responsible for the Stardalur magnetic anomaly spurred numerous international collaborations. Leo was a dedicated scientist always striving for the right answer,

not the simple solution. Low temperature magnetic measurements were made at the Institute for Rock Magnetism (IRM) at the University of Minnesota. The IRM is a U.S. National Multi-user Facility supported through the Instrumentation and Facilities program of the National Science Foundation, Earth Sciences Division, and by funding from the University of Minnesota. Magnetic measurements, SEM and EMP data were funded through the Institute for Geoscience and Petroleum, at NTNU. We thank Thomas Berndt and two anonymous reviewers for their helpful comments.

DATA AVAILABILITY

The data underlying this paper will be shared on reasonable request to the corresponding author.

REFERENCES

Balsley, J.R. & Buddington, A.F., 1958. Iron-titanium oxide minerals, rocks, and aeromagnetic anomalies of the Adirondack Area, New York, *Econ. Geol.,* **53**(7), 777–805.

Búason, D., 1971. Unpublished data on measurements of magnetic fields in Stardalur and magnetic properties of samples from drill hole no. 1, Tech. rep., University of Iceland.

Béguin, A. & Fabian, K., 2021. Demagnetization energy and internal stress in magnetite from temperature dependent hysteresis measurements, *Geophys. Res. Lett.,* **48**(24) , doi:10.1029/2021GL096147.

Bennett, E.N., Lissenberg, C.J. & Cashman, K.V., 2019. The significance of plagioclase textures in mid-ocean ridge basalt (Gakkel Ridge, Arctic Ocean), *Contrib. Mineral. Petrol.,* **174**(6) , doi:10.1007/s00410-019-1587-1.

Bleil, U., Hall, J.M., Johnson, H.P., Levi, S. & Schonharting, G., 1982. The natural magnetization of a 3-kilometer section of Icelandic crust, *J. geophys. Res.,* **87**(B8), 6569–6589.

Bowles, J.A., Lappe, S. L.L., Jackson, M.J., Arenholz, E. & Laan, G., 2019. Curie temperature enhancement and cation ordering in titanomagnetites: evidence from magnetic properties, XMCD, and Mössbauer spectroscopy, *Geochem. Geophys. Geosyst.,* **20,** 2272–2289.

Church, N.S., Fabian, K. & McEnroe, S.A., 2016. Nonlinear Preisach maps: detecting and characterizing separate remanent magnetic fractions in complex natural samples, *J. geophys. Res.,* **121**(12), 8373–8395.

Clark, D.A., 1997. Magnetic petrophysics and magnetic petrology: aids to geological interpretation of magnetic surveys, *J. Aust. Geol. Geophys.,* **17**(2), 83– 103.

Coe, R.S., Egli, R., Gilder, S.A. & Wright, J.P., 2012. The thermodynamic effect of nonhydrostatic stress on the Verwey transition, *Earth planet. Sci. Lett.,* **319–320,** 207–217.

Cromwell, G., Tauxe, L. & Halldórsson, S.A., 2015. New paleointensity results from rapidly cooled Icelandic lavas: implications for Arctic geomagnetic field strength, *J. geophys. Res.,* **120**(5), 2913–2934.

Crovisier, J.-L., Honnorez, J., Fritz, B. & Petit, J.-C., 1992. Dissolution of subglacial volcanic glasses from Iceland: laboratory study and modelling, *Appl. Geochem.,* **7,** 55–81.

Day, R., Fuller, M. & Schmidt, V.A., 1977. Hysteresis properties of titanomagnetites: grain-size and compositional dependence, *Phys. Earth planet. Inter.,* **13,** 260–267.

Draeger, U., Prevot, M., Poidras, T. & Riisager, J., 2006. Single-domain chemical, thermochemical and thermal remanences in a basaltic rock, *Geophys. J. Int.,* **166,** 12–32.

Dunlop, D.J., 2002. Theory and application of the Day plot (Mrs/Ms versus Hcr/Hc) 1. Theoretical curves and tests using titanomagnetite data, *J. geophys. Res.,* **107**(B3), 2056, doi:10.1029/2001JB000486.

Dunlop, D.J., 2014. High-temperature susceptibility of magnetite: a new pseudo-single-domain effect, *Geophys. J. Int.,* **199**(2), 707–716.

Dunlop, D.J. & Özdemir, O., 2018. Remanence cycling of 0.6–135 μm magnetites across the Verwey transition, *Earth, Planets Space,* **70**(1), doi:10.1186/s40623-018-0928-z.

Eason, D.E. & Sinton, J.M., 2009. Lava shields and fissure eruptions of the western volcanic zone, Iceland: evidence for magma chambers and crustal interaction, *J. Volc. Geotherm. Res.,* **186**(3–4), 331–348.

Egli, R., 2013. VARIFORC: an optimized protocol for calculating non-regular first-order reversal curve (FORC) diagrams, *Global planet. Change,* **110,** 302–320.

Fabian, K., 2009. Thermochemical remanence acquisition in single-domain particle ensembles: a case for possible overestimation of the geomagnetic paleointensity, *Geochem. Geophys. Geosyst.,* **10**(6), doi:10.1029/2009GC002420.

Fabian, K. & Shcherbakov, V.P., 2020. The magnetization of the ocean floor: stress and fracturing of titanomagnetite particles by low-temperature oxidation, *Geophys. J. Int.,* **221**(6), 2104–2112.

Fabian, K., McEnroe, S.A., Robinson, P. & Shcherbakov, V.P., 2008. Exchange bias identifies lamellar magnetism as the origin of the natural remanent magnetization in titanohematite with ilmenite exsolution from Modum, Norway, *Earth planet. Sci. Lett.,* **268**(3-4), 339–353.

Fabian, K., Shcherbakov, V.P. & McEnroe, S.A., 2013. Measuring the Curie temperature, *Geochem. Geophys. Geosyst.,* **14**(4), 947–961.

Faure, F., Trolliard, G., Nicollet, C. & Montel, J.-M., 2003. A developmental model of olivine morphology as a function of the cooling rate and the degree of undercooling, *Contrib. Mineral. Petrol.,* **145**(2), 251–263.

Fleet, M.E., 1984. The structure of magnetite: two annealed natural magnetites, $Fe_{3.005}O_4$ and $Fe_{2.96}Mg_{0.04}O_4$, *Acta Crystallogr. Sect. C Cryst. Struct. Commun.,* **40**(9), 1491–1493.

Franzson, H., Guðfinnsson, G.H., Helgadóttir, H.M. & Frolova, J., 2010. Porosity, density and chemical composition relationships in altered Icelandic hyaloclastites, in *Water-Rock Interaction,* pp. 199–20, eds Birkle, P. & Torres-Alvarado, I.S., Taylor & Francis Group.

Friðleifsson, I., 1973. Petrology and structure of the Esja Quaternary volcanic region, southwest Iceland, *PhD thesis*, University of Oxford.

Friðleifsson, I.B. & Kristjánsson, L., 1972. The Stardalur magnetic anomaly, SW-Iceland, *Jökull,* **22,** 69–78.

Friðleifsson, I.B. & Tómasson, J., 1972. Jarðhitarannsóknir á stardalssvæðinu 1969-1971 (geological investigations around the Stardalur farm in 1969-1971, in Icelandic), Tech. rep., National Energy Authority and the Reykjavik Municipal Geothermal Supply Co., Reykjavík.

Gardner, L.R., 1980. Mobilization of al and ti during weathering—isovolumetric geochemical evidence, *Chem. Geol.,* **30**(1–2), 151–165.

Geirsdóttir, Á., Miller, G.H. & Andrews, J.T., 2007. Glaciation, erosion, and landscape evolution of Iceland, *J. Geodyn.,* **43**(1), 170–186.

Goguitchaichvili, A., Prévot, M. & Camps, P., 1999. No evidence for strong fields during the R3-N3 Icelandic geomagnetic reversal, *Earth planet. Sci. Lett.,* **167**(1-2), 15–34.

Gunnlaugsson, H., Helgason, O., Kristjánsson, L. & Steinthórsson, S., 2004. Samanburdur Mössbauerrófa af bergi frá Íslandi og Mars (comparison of Mössbauer spectra of rocks from Iceland and Mars, in Icelandic with English summary), *Raust,* **2**(2), 63–70.

Gunnlaugsson, H.P., Helgason, O., Kristjánsson, L., Nørnberg, P., Rasmussen, H., Steinbórsson, S. & Weyer, G., 2006. Magnetic properties of olivine basalt: application to Mars, *Phys. Earth planet. Inter.s,* **154,** 276–289.

Harrison, R.J. & Feinberg, J.M., 2008. FORCinel: an improved algorithm for calculating first-order reversal curve distributions using locally weighted regression smoothing, *Geochem. Geophys. Geosyst.,* **9**(5) , doi:10.1029/2008gc001987.

Helgason, O., Steinthórsson, S., Madsen, M.B. & Mørup, S., 1990. On anomalously magnetic basalt lavas from Stardalur Iceland, *Hyperfine Interact.,* **57**(1–4), 2209–2214.

Hodych, J., 1996. Inferring domain state from magnetic hysteresis in high coercivity dolerites bearing magnetite with ilmenite lamellae, *Earth planet. Sci. Lett.,* **142,** 523–533.

Jackson, M.J. & Moskowitz, B., 2020. On the distribution of Verwey transition temperatures in natural magnetites, *Geophys. J. Int.,* **224**(2), 1314–1325.

Jakobsson, S.P., 1972. Chemistry and distribution pattern of recent basaltic rocks in Iceland. Lithos, 5(4), 365-386..

Jercinovic, M., Keil, K., Smith, M. & Schmitt, R., 1990. Alteration of basaltic glasses from north-central british columbia, canada, *Geochim. Cosmochim. Acta,* **54**(10), 2679–2696.

Kanakiya, S., Turner, G.M., Rowe, M.C., Adam, L. & Lindsay, J.M., 2021. High remanent magnetization measured in hydrothermally altered lavas, *Geophys. Res. Lett.,* **48**(23), doi:10.1029/2021gl095732.

Kneller, E., 1962. *Ferromagnetismus,* Springer.

Kristjansson, L., 2002. Estimating properties of the paleomagnetic field from Icelandic lavas, *Phys. Chem. Earth, Parts A/B/C,* **27**(25–31), 1205–1213.

Kristjánsson, L., 1970. Paleomagnetism and magnetic surveys in Iceland, *Earth planet. Sci. Lett.,* **8**(2), 101–108.

Kristjánsson, L., 2013. The Stardalur magnetic anomaly, SW-Iceland: a review of research in 1968–2012, *Jokull,* **63,** 1–16.

Kristjánsson, L. & Jónsson, G., 2017. A total-field magnetic anomaly map of the Reykjanes peninsula, Southwest Iceland, *Jökull,* **67,** 43–49.

Kristjánsson, L., Friðleifsson, I.B. & Watkins, N., 1980. Stratigraphy and paleomagnetism of the Esja, Eyrarfjall and Akrafjall Mountains, SW-Iceland, *J. Geophys.,* **47,** 31–42.

Lascu, I., Einsle, J.F., Ball, M.R. & Harrison, R.J., 2018. The vortex state in geologic materials: a micromagnetic perspective, *J. geophys. Res.,* **123**(9), 7285–7304.

Lee, J., Kwon, S.G., Park, J.-G. & Hyeon, T., 2015. Size dependence of metal–insulator transition in stoichiometric Fe_3O_4 nanocrystals, *Nano Lett.,* **15**(7), 4337–4342.

Lindsley, D.H., 1981. Some experiments pertaining to the magnetite–ulvöspinel miscibility gap, *Am. Mineral.,* **66**(7–8), 759–762.

Liu, Q., Banerjee, S.K., Jackson, M.J., Chen, F., Pan, Y. & Zhu, R., 2004. Determining the climatic boundary between the Chinese loess and palaeosol: evidence from aeolian coarse-grained magnetite, *Geophys. J. Int.,* **156**(2), 267–274.

McCammon, C.A., McEnroe, S.A., Robinson, P., Fabian, K. & Burton, B.P., 2009. High efficiency of natural lamellar remanent magnetisation in single grains of ilmeno-hematite calculated using Mössbauer spectroscopy, *Earth planet. Sci. Lett.,* **288**(1-2), 268–278.

McClelland-Brown, E., 1982. Discrimiation of TRM and CRM by blocking-temperature spectrum analysis, *Phys. Earth planet. Inter.,* **30,** 405–414.

McEnroe, S.A. & Brown, L.L., 2000. A closer look at remanence-dominated aeromagnetic anomalies: rock magnetic properties and magnetic mineralogy of the Russell belt microcline-sillimanite gneiss, northwest Adirondack Mountains, New York, *J. geophys. Res.,* **105**(B7), 16 437–16 456.

McEnroe, S.A., Robinson, P. & Panish, P., 2000. Chemical and petrographic characterization of ilmenite and magnetite in oxide-rich cumulates of the Sokndal Region, Rogaland, Norway, *Norweg. Geol. Surv. Bull.,* **436,** 49–56.

McEnroe, S.A., Harrison, R.J., Robinson, P., Golla, U. & Jercinovic, M.J., 2001. Effect of fine-scale microstructures in titanohematite on the acquisition and stability of natural remanent magnetization in granulite facies metamorphic rocks, southwest Sweden: implications for crustal magnetism, *J. geophys. Res.,* **106**(B12), 30 523–30 546.

Muxworthy, A.R. & Dunlop, D.J., 2002. First-order reversal curve (FORC) diagrams for pseudo-single-domain magnetites at high temperature, *Earth planet. Sci. Lett.,* **203**(1), 369–382.

Néel, L., 1955. Some theoretical aspects of rock-magnetism, *Adv. Phys.,* **4,** 191–243.

Newell, A.J., 2005. A high-precision model of first-order reversal curve (FORC) functions for single-domain ferromagnets with uniaxial anisotropy, *Geochem. Geophys. Geosyst.,* **6**(5), Q05010 , doi:10.1029/2004GC000877.

Nikolaisen, E.S., Harrison, R., Fabian, K. & McEnroe, S.A., 2020. Hysteresis of natural magnetite ensembles: micromagnetics of silicate-hosted magnetite inclusions based on focused-ion-beam nanotomography, *Geochem. Geophys. Geosyst.,* **21**(11), doi:10.1029/2020gc009389.

Özdemir, O. & Dunlop, D.J., 2010. Hallmarks of maghemitization in low-temperature remanence cycling of partially oxidized magnetite nanoparticles, *J. geophys. Res.,* **115**(B2) , doi:10.1029/2009jb006756.

Pasquarè, F. & Tibaldi, A., 2007. Structure of a sheet-laccolith system revealing the interplay between tectonic and magma stresses at Stardalur volcano, Iceland, *J. Volc. Geotherm. Res.,* **161**(1–2), 131–150.

Penny, C., Muxworthy, A.R. & Fabian, K., 2019. Mean-field modelling of magnetic nanoparticles: the effect of particle size and shape on the Curie temperature, *Phys. Rev. B,* **99,** 174414 , doi:10.1103/PhysRevB.99.174414.

Petrovský, E. & Kapička, A., 2006. On determination of the curie point from thermomagnetic curves, *J. geophys. Res.,* **111**(B12), 1–10.

Pike, C.R., Roberts, A.P. & Verosub, K.L., 1999. Characterizing interactions in fine magnetic particle systems using first order reversal curves, *J. appl. Phys.,* **85**(9), 6660–6667.

Pike, C.R., Roberts, A.P. & Dekkers, M.J., 2001. An investigation of multi-domain hysteresis mechanisms using FORC diagrams, *Phys. Earth planet. Inter.,* **126**(1–2), 11–25.

Pálmason, G., 2005. Jarðhitabók (geothermics, in Icelandic), Tech. rep., Hið íslenska bókmenntafélag, Reykjavík.

Roberts, A.P., Pike, C.R. & Verosub, K.L., 2000. First-order reversal curve diagrams: a new tool for characterizing the magnetic properties of natural samples, *J. geophys. Res.,* **105**(B12), 28 461–28 475.

Robinson, P., Harrison, R.J., McEnroe, S.A. & Hargraves, R.B., 2002. Lamellar magnetism in the haematite–ilmenite series as an explanation for strong remanent magnetization, *Nature,* **418**(6897), 517–520.

Robinson, P., Harrison, R.J. & McEnroe, S.A., 2006. Fe^{2+}/Fe^{3+} charge ordering in contact layers of lamellar magnetism: bond valence arguments, *Am. Mineral.,* **91**(1), 67–72.

Robinson, P., McEnroe, S.A., Miyajima, N., Fabian, K. & Church, N., 2016. Remanent magnetization, magnetic coupling, and interface ionic configurations of intergrown rhombohedral and cubic Fe-Ti oxides: a short survey, *Am. Mineral.,* **101**(3-4), 518–530.

Salas, P., Ruprecht, P., Hernández, L. & Rabbia, O., 2021. Out-of-sequence skeletal growth causing oscillatory zoning in arc olivines, *Nat. Commun.,* **12**(1) , doi:10.1038/s41467-021-24275-6.

Shcherbakov, V.P., Fabian, K., Sycheva, N.K. & McEnroe, S.A., 2012. Size and shape dependence of the magnetic ordering temperature in nanoscale magnetic particles, *Geophys. J. Int.,* **191**(3), 954–964.

Shea, T., Lynn, K.J. & Garcia, M.O., 2015. Cracking the olivine zoning code: distinguishing between crystal growth and diffusion, *Geology,* **43**(10), 935–938.

Sigurgeirsson, T., 1970–1985. Aeromagnetic profile maps of Iceland in scale 1:250,000, Tech. rep., University of Iceland.

Smith, K.L., 1987. Weathering of basalt: formation of iddingsite, *Clays Clay Miner.,* **35**(6), 418–428.

Sparks, R., Meyer, P. & Sigurdsson, H., 1980. Density variation amongst mid-ocean ridge basalts: implications for magma mixing and the scarcity of primitive lavas, *Earth planet. Sci. Lett.,* **46**(3), 419–430.

SteinÞórsson, S. & Sigvaldason, G., 1971. Skýrsla um bergfræðirannsóknir við Stardal (Report on petrological studies on the Stardalur drill core, in Icelandic), Tech. rep., Science Institute, University of Iceland.

SteinÞórsson, S., Helgason, O., Madsen, M.B., Koch, C.B., Bentzon, M.D. & Mørup, S., 1992. Maghemite in Icelandic basalts, *Mineral. Mag.,* **56**(383), 185–199.

ter Maat, G.W., Fabian, K., Church, N.S. & McEnroe, S.A., 2020. Separating geometry from stress-induced remanent magnetization in magnetite with ilmenite lamellae from the Stardalur basalts, Iceland, *Geochem. Geophys. Geosyst.,* **21,** doi:10.1029/2019gc008761.

Tonti-Filippini, J. A.D. & Brown, M.C., 2019. The Iceland palaeomagnetism database (ICEPMAG), *Earth, Planets Space,* **71**(1), doi:10.1186/s40623-019-1060-4.

Vahle, C., Kontny, A., Gunnlaugsson, H.P. & Kristjansson, L., 2007. The Stardalur magnetic anomaly revisited—new insights into a complex cooling and alteration history, *Phys. Earth planet. Inter.,* **163,** 119–141.

Vincent, E., Wright, J., Chavallier, R. & Mathieu, S., 1957. Heating experiments on some natural titaniferous magnetites, *Mineral. Mag.,* **31**(4), 624–655.

Walz, F., 2002. The Verwey transition—a topical review, *J. Phys.: Condens. Matter,* **14**(12), R285–R340.

Wechsler, B.A. & Prewitt, C.T., 1984. Crystal structure of ilmenite ($FeTiO_3$) at high temperature and at high pressure, *Am. Mineral.,* **69,** 176–185.

Welsch, B., Hammer, J. & Hellebrand, E., 2014. Phosphorus zoning reveals dendritic architecture of olivine, *Geology,* **42**(10), 867–870.

Yamamoto, Y., 2006. Possible TCRM acquisition of the Kilauea 1960 lava, Hawaii: failure of the Thellier paleointensity determination inferred from equilibrium temperature of the Fe-Ti oxide, *Earth, Planets Space,* **58**(8), 1033–1044.

Yamamoto, Y., Tsunakawa, H. & Shibuya, H., 2003. Palaeointensity study of the Hawaiian 1960 lava: implications for possible causes of erroneously high intensities, *Geophys. J. Int.,* **153**(1), 263–276.

Yu, Y., 2006. How accurately can NRM/SIRM determine the ancient planetary magnetic field intensity?, *Earth planet. Sci. Lett.,* **250**(1–2), 27–37.

SUPPORTING INFORMATION

Supplementary data are available at *GJI* online.

Figure S1. Downcore plots of backfield-curve quantiles for the Stardalur drill core. Each line provides the coercivity at which a certain fraction q of the remanent magnetization is reversed. The red line for $q = 0.5$ corresponds to B_{cr}. The interval between the $q = 0.1$ and the $q = 0.9$ quantiles of the coercivity distribution for most Stardalur samples (besides ST36) is within the range of 5–100 mT.

Figure S2. Néel plot of M_{rs}/M_s versus H_c for the Stardalur samples, coloured by NRM/M_{rs} (here using hysteresis loop, but equivalent to NRM/SIRM). Dashed line is magnetite trend calculated by Hodych (1996).

Figure S3. Néel plot of M_{rs}/M_s versus H_c for the Stardalur samples, coloured by NRM. Dashed line is magnetite trend calculated by Hodych (1996).

Figure S4. Néel plot of M_{rs}/M_s versus H_c for the Stardalur samples, coloured by density. Dashed line is magnetite trend calculated by Hodych (1996).

Figure S5. Plot of NRM versus magnetite content, calculated from M_s of hysteresis loops and coloured by density. The correlation between total NRM and magnetite content is weak, confirming that efficiency is the dominant parameter controlling NRM values in the Stardalur basalts.

Figure S6. NRM efficiency (NRM/M_s) versus M_{rs}/M_s ratio, coloured by total NRM.

Figure S7. Non-linear Preisach maps (Church *et al.* 2016) of selected Stardalur samples, sorted by ascending remanence efficiency (NRM/M_s). Lower efficiency appears to be related to a low-coercivity tail below 10 mT of the IRM acquisition curve (red line above the diagrams). Alteration in ST78 rather generates a high-coercivity tail above 100 mT. High efficiency rather occurs in samples with focused coercivity distributions between 10 and 100 mT, but does not require a narrow distribution of interaction fields. These observations are in agreement with fine-scale exsolution and stress stabilization of the remanence carriers. They exclude any importance of large MD or non-interacting SD particles for the unusual NRM efficiency which would either be indicated by low coercivities and wide spread of the Preisach distribution, or by a much narrower prominent central ridge.

Figure S8. First-order reversal curve diagrams of selected Stardalur samples, sorted by ascending NRM efficiency NRM/M_s. Also indicated are the remanence normalized NRM efficiencies defined by NRM/M_r, and percentile rank of each parameter with respect to the total Stardalur data set. The FORCs of the lowest three NRM/M_s samples have a more pronounced MD contribution, but note that ST80 still has a high efficiency in terms of NRM/M_r. Note also that the relatively pronounced and narrow SD ridge in ST87 does not induce a high NRM/M_s.

Figure S9. First-order reversal curve diagrams of highly efficient Stardalur samples. The most efficient sample in terms of NRM/M_s shows a clear SD like central ridge, and has much lower efficiency in terms of NRM/M_r. Samples with high efficiencies in both normalizations appear to have a focused H_c distribution and a wider H_u distribution, which supports the results from the Preisach distributions and agrees with a finely exsolved and maybe stressed magnetite carrier.

Table S1. Sampling, NRM and magnetic susceptibility (MS) of the Stardalur drill core, reported by Búason (1971).

Table S2. Verwey transition temperatures (T_V), calculated from measurements of different magnetic parameters.

Please note: Oxford University Press is not responsible for the content or functionality of any supporting materials supplied by the authors. Any queries (other than missing material) should be directed to the corresponding author for the paper.